J. Fluid Mech. (2020), *vol*. 899, A15. © The Author(s), 2020.
Published by Cambridge University Press
doi:10.1017/jfm.2020.465

Thermodynamically consistent phase-field modelling of contact angle hysteresis

Pengtao Yue†

Department of Mathematics, Virginia Tech, Blacksburg, VA 24061, USA

(Received 11 February 2020; revised 28 May 2020; accepted 4 June 2020)

In the phase-field description of moving contact line problems, the two-phase system can be described by free energies, and the constitutive relations can be derived based on the assumption of energy dissipation. In this work we propose a novel boundary condition for contact angle hysteresis by exploring wall energy relaxation, which allows the system to be in non-equilibrium at the contact line. Our method captures pinning, advancing and receding automatically without the explicit knowledge of contact line velocity and contact angle. The microscopic dynamic contact angle is computed as part of the solution instead of being imposed. Furthermore, the formulation satisfies a dissipative energy law, where the dissipation terms all have their physical origin. Based on the energy law, we develop an implicit finite element method that is second order in time. The numerical scheme is proven to be unconditionally energy stable for matched density and zero contact angle hysteresis, and is numerically verified to be energy dissipative for a broader range of parameters. We benchmark our method by computing pinned drops and moving interfaces in the plane Poiseuille flow. When the contact line moves, its dynamics agrees with the Cox theory. In the test case of oscillating drops, the contact line transitions smoothly between pinning, advancing and receding. Our method can be directly applied to three-dimensional problems as demonstrated by the test case of sliding drops on an inclined wall.

Key words: drops, contact lines, computational methods

1. Introduction

In reality, most solid surfaces are intrinsically rough or chemically heterogeneous. As a consequence, the contact line may get pinned at the topological or chemical defects and results in non-unique values in the static contact angle (also known as the equilibrium contact angle). The maximum and minimum static contact angles are referred to as the advancing (θ_A) and receding (θ_R) angles; their difference $\theta_A - \theta_R$ is known as the contact angle hysteresis (CAH) (Dussan V. 1979; Quéré 2008). There has been a sizable body of literature exploring the underlying physics of CAH (e.g. Extrand 2002; Gao & McCarthy 2006; Whyman, Bormashenko & Stein 2008; Makkonen 2017; Wu & Ma 2017). The readers are referred to Eral, 't Mannetje & Oh (2013) and Extrand (2016) for recent reviews on this topic. It should be noted that CAH is even observed on inherently smooth and

† Email address for correspondence: ptyue@vt.edu

https://doi.org/10.1017/jfm.2020.465 Published online by Cambridge University Press

homogeneous surfaces (Rahimi & Ward 2005). Thus, CAH is ubiquitous and should be considered in contact line simulations if possible.

Contact angle hysteresis can be computationally reproduced if topological or chemical heterogeneities on the solid wall are sufficiently resolved. For example, the phase-field method has been successfully used to investigate CAH on chemically heterogeneous (Kusumaatmaja & Yeomans 2007; Wylock *et al.* 2012) surfaces and topologically rough (Luo, Wang & Cai 2017) surfaces. There has also been many theoretical works aiming to predict advancing and receding angles based on chemical and topological patterns (Iwamatsu 2006; Xu & Wang 2011, 2013).

We do not intend to explore the microscopic origin of contact angle hysteresis. Instead, we focus on numerical simulations at length scales much greater than the characteristic scales of the topological or chemical heterogeneities. At this macroscopic level, the solid surface can be considered smooth and θ_A and θ_R can be treated as measurable constants associated with the given system. The contact line is pinned if the contact angle is within the hysteresis window $[\theta_R, \theta_A]$ and moves if otherwise. This is much more computationally affordable than treating the surface as topologically or chemically patterned. The most popular approach for CAH was developed by Spelt (2005) for a level-set method. In this approach, an intermediate contact angle is obtained such that the contact line is pinned. If this angle is within the hysteresis window, the solution is accepted; otherwise, the solution is abandoned and the contact line is moved with prescribed contact angles. This approach was widely adopted and later extended to the phase field (Ding & Spelt 2008; Huang, Huang & Wang 2014), volume-of-fluid (Dupont & Legendre 2010; Maglio & Legendre 2014; Linder *et al.* 2015) and lattice Boltzmann methods (Ba *et al.* 2013; Wang, Huang & Lu 2013; Liu *et al.* 2015). However, this approach requires ghost cells outside the boundary to impose the contact angle condition or pin the contact line, which can be challenging on curved boundaries and unstructured meshes. Furthermore, to capture slip lengths much smaller than the mesh size, a macroscale model has to be used to find the dynamic contact angle on the boundary. This requires an accurate evaluation of the contact line velocity, which can be tricky to compute due to complications from the wedge flow (Linder *et al.* 2015; Afkhami *et al.* 2018). Recently, Shin, Chergui & Juric (2018) introduced an extended interface approach to model CAH in a front tracking method, where the generalized Navier boundary condition (GNBC) (Qian, Wang & Sheng 2003) was adopted for the moving contact line. This method, however, still requires ghost cells to impose CAH condition and a hydrodynamic model to impose the dynamic contact angle.

The phase-field method, also known as the diffuse-interface method, has turned into a favourable numerical tool for moving contact line problems since the pioneering work of Jacqmin (2000). The built-in Cahn–Hilliard diffusion automatically regularizes the stress singularity at the moving contact line. Another benefit is its energy formulation, which can be used to guide the design of energy stable numerical schemes, such as convex splitting (Eyre 1998), linear stabilization (Shen & Yang 2010; Shen, Yang & Yu 2015; Yu & Yang 2017), invariant energy quadratization (Yang 2016) and scalar auxiliary variable (Shen, Xu & Yang 2018) methods. In this work we will develop a boundary condition for CAH based on wall energy relaxation. Our method does not require ghost cells or the evaluation of contact angle or contact line velocity. More importantly, the energy formulation is preserved. It should be noted that, in the literature, the first phase-field model for CAH was proposed by Vedantam & Panchagnula (2007): an Allen–Cahn equation on the solid surface was used to model liquid spreading. But no fluid flow was considered and the whole set-up was purely phenomenological. It is thus totally different from the current work.

https://doi.org/10.1017/jfm.2020.465 Published online by Cambridge University Press

The rest of this paper is organized as follows. We first introduce the governing equations for contact line problems without CAH in § 2. We then develop the CAH model in § 3, where we also prove the dissipative energy law. The weak form together with numerical discretization is provided in § 4. Numerical results including benchmarks are given in § 5, where we also come up with a computational strategy for CAH. For the reader's convenience, the following technical topics are included in the appendices: the derivation of wall energy is given in appendix A; constitutive relations, including GNBC, are derived based on the second law of thermodynamics in appendix B; compressibility caused by Cahn–Hilliard diffusion is discussed in appendix C.

2. Phase-field method for moving contact lines

We consider an incompressible two-phase system of Newtonian fluids in domain Ω and in contact with a solid wall $\partial\Omega_w$ which is a subset of the domain boundary $\partial\Omega$. We introduce a phase-field variable ϕ, which changes from $+1$ in fluid 1 to -1 in fluid 2. The total free energy, including the kinetic energy, can be written as

$$\mathcal{F} = \int_\Omega \left(f_m(\phi, \nabla\phi) + \frac{1}{2}\rho|\boldsymbol{u}|^2 \right) \mathrm{d}\boldsymbol{x} + \int_{\partial\Omega_w} f_w(\phi)\,\mathrm{d}s, \tag{2.1}$$

where

$$f_m(\phi, \nabla\phi) = \lambda\left(\frac{1}{2}|\nabla\phi|^2 + f_0(\phi)\right) \tag{2.2}$$

is the mixing energy per unit volume (Cahn & Hilliard 1958),

$$f_0(\phi) = \frac{(\phi^2-1)^2}{4\epsilon^2} \tag{2.3}$$

is the double-well potential, and

$$f_w(\phi) = -\sigma\cos\theta_S \frac{\phi(3-\phi^2)}{4} \tag{2.4}$$

is the surface energy per unit area on the wall (Cahn 1977; Jacqmin 2000). Here ρ is the fluid density, $\boldsymbol{u}$ is the fluid velocity, λ is the mixing energy density, ϵ is the capillary width, σ is the surface tension and θ_S is the static contact angle (also known as the equilibrium contact angle) defined in fluid 1 ($\phi = 1$). For a one-dimensional diffuse interface in equilibrium, we have (Yue *et al.* 2004)

$$\sigma = \frac{2\sqrt{2}}{3}\frac{\lambda}{\epsilon} \tag{2.5}$$

and

$$\phi(x) = \tanh\left(\frac{x}{\sqrt{2}\epsilon}\right), \tag{2.6}$$

where we have assumed that the diffuse interface is centred at $x = 0$. The derivation of f_w can be found in appendix A.

https://doi.org/10.1017/jfm.2020.465 Published online by Cambridge University Press

The free energy (2.1) leads to the following coupled system of Navier–Stokes and Cahn–Hilliard equations:

$$\rho\left(\frac{\partial \boldsymbol{u}}{\partial t}+\boldsymbol{u}\cdot\nabla\boldsymbol{u}\right)+\boldsymbol{J}\cdot\nabla\boldsymbol{u}=-\nabla p+\nabla\cdot\boldsymbol{\tau}+G\nabla\phi+\rho\boldsymbol{g}, \tag{2.7}$$

$$\nabla\cdot\boldsymbol{u}=0, \tag{2.8}$$

$$\frac{\partial\phi}{\partial t}+\boldsymbol{u}\cdot\nabla\phi=\nabla\cdot(M\nabla G), \tag{2.9}$$

$$G=\lambda(-\Delta\phi+f_0'(\phi)). \tag{2.10}$$

Here ρ is the density, $\boldsymbol{u}$ is the volume-averaged velocity, $\boldsymbol{J}$ is a diffusive flux caused by the discrepancy between $\boldsymbol{u}$ and the mass-averaged velocity (Abels, Garcke & Grün 2012), $\boldsymbol{\tau}=\mu(\nabla\boldsymbol{u}+(\nabla\boldsymbol{u})^T)$ is the viscous stress, μ is the viscosity and G is the chemical potential. It should be noted that the Cahn–Hilliard equation is split into two second order equations (2.9) and (2.10). This is a common treatment in finite element methods (Yue *et al.* 2006; Khatavkar, Anderson & Meijer 2007*b*), because the C^0 finite elements cannot handle fourth-order derivatives directly. These equations are complemented by the following boundary conditions:

$$\boldsymbol{u}=\boldsymbol{u}_w \quad \text{on } \partial\Omega_w, \tag{2.11}$$

$$\boldsymbol{n}\cdot\nabla G=0 \quad \text{on } \partial\Omega, \tag{2.12}$$

$$\frac{\partial\phi}{\partial t}+\boldsymbol{u}\cdot\nabla\phi=-\Gamma L(\phi,\nabla\phi) \quad \text{on } \partial\Omega_w, \tag{2.13}$$

$$\boldsymbol{n}\cdot\nabla\phi=0 \quad \text{on } \partial\Omega\backslash\partial\Omega_w. \tag{2.14}$$

Here $\boldsymbol{u}_w$ is the wall velocity, Γ is a positive phenomenological parameter that controls the rate of wall energy relaxation and

$$L(\phi,\nabla\phi)=\lambda\boldsymbol{n}\cdot\nabla\phi+f_w'(\phi) \tag{2.15}$$

is the wall potential. Equations (2.11)–(2.13) correspond to the no-slip, zero diffusive flux and wall energy relaxation conditions, respectively. Equation (2.14) corresponds to a homogeneous natural boundary condition, which does not require any special attention in the finite element methods. The interested readers are referred to appendices B and C for the derivation of these equations. On $\partial\Omega\backslash\partial\Omega_w$, i.e. boundaries other than solid walls, additional velocity or stress conditions are required depending on the particular problem.

In our phase-field formulation, ϕ is related to volume fraction and the mixture properties are computed by

$$\rho(\phi)=\frac{1+\phi}{2}\rho_1+\frac{1-\phi}{2}\rho_2, \quad \mu(\phi)=\frac{1+\phi}{2}\mu_1+\frac{1-\phi}{2}\mu_2, \tag{2.16a,b}$$

where subscripts '$_1$' and '$_2$' denote the properties of the pure fluids 1 and 2, respectively. Then, according to (B 13) and (C 4), the diffusive mass flux can be written as

$$\boldsymbol{J}=-\frac{\rho_1-\rho_2}{2}M\nabla G. \tag{2.17}$$

The wall energy relaxation (2.13), together with the no-slip condition (2.11), is a special case of GNBC. It works together with interface mobility to generate the desired slip length

https://doi.org/10.1017/jfm.2020.465 Published online by Cambridge University Press

(Yue & Feng 2011). According to Carlson, Do-Quang & Amberg (2011), the wall energy relaxation accounts for the dissipation due to the reorganization of molecules at the contact line.

For a planar interface, θ_S is recovered exactly if $L = 0$, i.e. when the system is in equilibrium at the contact line. Equation (2.13) allows the contact line to deviate from equilibrium, i.e. $L \neq 0$ when the contact line moves. This causes the actual microscopic contact angle measured at the wall (see figure 5*b*), termed the dynamic contact angle θ_D, to deviate from θ_S. This deviation has been confirmed by various molecular-dynamics studies (Ren & E 2007; Fernández-Toledano *et al.* 2019). Alternatively, if we assume that the microscopic angle stays at its equilibrium value θ_S then θ_D in the phase-field model can be viewed as the interface angle at a distance of $\mathcal{O}(l_D)$ to the contact line, where $l_D = \sqrt{M\mu}$ is the diffusion length and μ is an effective viscosity (Yue, Zhou & Feng 2010; Yue & Feng 2011). Numerically, this θ_D plays a role similar to the intermediate angle in the macroscale approach of Spelt (2005) and the numerical angle in the mesh-independent volume-of-fluid method of Afkhami, Zaleski & Bussmann (2009). The major difference is that our θ_D is automatically obtained from the phase-field simulations instead of being manually imposed based on external models such as the hydrodynamic model developed by Voinov (1976) and Cox (1986).

3. Contact angle hysteresis

3.1. *Boundary condition for contact angle hysteresis*

On the solid wall, the motion of the contact line is directly related to the variation of ϕ: the contact line advances if $\mathrm{D}\phi/\mathrm{D}t > 0$ (i.e. the region previously occupied by $\phi = -1$ is now occupied by $\phi = 1$), recedes if $\mathrm{D}\phi/\mathrm{D}t < 0$ and is pinned if $\mathrm{D}\phi/\mathrm{D}t = 0$. Here $\mathrm{D}/\mathrm{D}t = \partial/\partial t + \boldsymbol{u}\cdot\nabla$ denotes the material derivative and, in particular, $\mathrm{D}/\mathrm{D}t = \partial/\partial t$ on fixed walls. Meanwhile, θ_D is embedded in the $\boldsymbol{n}\cdot\nabla\phi$ term of the wall potential L. We have $L < 0$ if $\theta_D > \theta_S$, $L > 0$ if $\theta_D < \theta_S$ and $L = 0$ if $\theta_D = \theta_S$. Interested readers are referred to appendix A for more details. Thus, we recover the criterion for contact line motion: contact line advances (or recedes) if $\theta_D > \theta_S$ (or $\theta_D < \theta_S$) and is pinned if $\theta_D = \theta_S$.

When CAH exists, the static contact angle has non-unique values, the maximum of which is the advancing contact angle θ_A and the minimum of which is the receding contact angle θ_R. The contact line advances if $\theta_D > \theta_A$, recedes if $\theta_D < \theta_R$ and is pinned if $\theta_R \leq \theta_D \leq \theta_A$, as illustrated in figure 1.

For convenience, we rewrite the wall energy as

$$f_w(\phi;\theta) = -\sigma\cos\theta\,\frac{\phi(3-\phi^2)}{4}, \tag{3.1}$$

where the contact angle θ is included as a parameter. For the physically relevant range $\phi \in [-1, 1]$,

$$f_w'(\phi;\theta) = -\frac{3}{4}\sigma\cos\theta(1-\phi^2) \tag{3.2}$$

is an increasing function in θ, where $'$ denotes the derivative in the first argument. It follows that $L(\phi, \nabla\phi;\theta) = \lambda\boldsymbol{n}\cdot\nabla\phi + f_w'(\phi;\theta)$ is also an increasing function in θ. For brevity, we denote $L(\phi, \nabla\phi;\theta_A)$ by L_A and $L(\phi, \nabla\phi;\theta_R)$ by L_R.

For a contact line with dynamic angle θ_D, the contact line would be in equilibrium if θ_D were also the static contact angle; it follows that $L(\phi, \nabla\phi;\theta_D) = 0$, i.e. $\lambda\boldsymbol{n}\cdot\nabla\phi = -f_w'(\phi;\theta_D)$. This is exactly (A 7) in appendix A. Then the relations between θ_D, θ_A and θ_R can be mapped to the relations between the wall potentials associated with these angles:

https://doi.org/10.1017/jfm.2020.465 Published online by Cambridge University Press

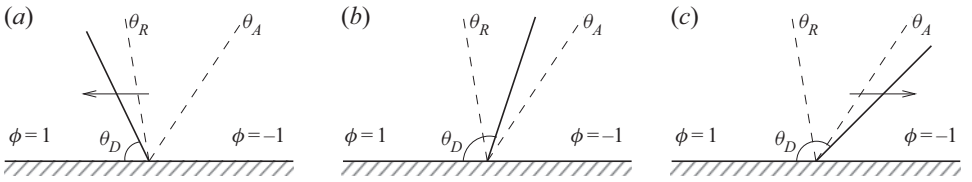


FIGURE 1. Different states of a contact line with CAH. We define the advancing and receding states with respect to the $\phi = 1$ fluid: (*a*) receding, $\theta_D < \theta_R$, (*b*) pinned, $\theta_R \leq \theta_D \leq \theta_A$ and (*c*) advancing, $\theta_D > \theta_A$.

(i) advancing contact line ($\mathrm{D}\phi/\mathrm{D}t > 0$) $\Leftrightarrow$ $\theta_D > \theta_A > \theta_R \Leftrightarrow 0 > L_A > L_R$;
(ii) receding contact line ($\mathrm{D}\phi/\mathrm{D}t < 0$) $\Leftrightarrow$ $\theta_A > \theta_R > \theta_D \Leftrightarrow L_A > L_R > 0$;
(iii) pinned contact line ($\mathrm{D}\phi/\mathrm{D}t = 0$) $\Leftrightarrow$ $\theta_A \geq \theta_D \geq \theta_R \Leftrightarrow L_A \geq 0 \geq L_R$.

Apparently, the state (advancing, receding or pinned) of the contact line can be determined by comparing the values of L_A and L_R. This motivates the following equation in place of (2.13) on $\partial\Omega_w$:

$$\frac{\partial \phi}{\partial t} + \boldsymbol{u} \cdot \nabla \phi = -\Gamma \tilde{L}. \tag{3.3}$$

Here

$$\tilde{L} = \mathrm{minmod}(L_A, L_R). \tag{3.4}$$

We use the minmod function

$$\mathrm{minmod}(a, b) = \begin{cases} \mathrm{sign}(a)\,\min(|a|, |b|) & \text{if } ab > 0, \\ 0 & \text{otherwise,} \end{cases}$$

which returns the argument with the smaller magnitude if both arguments have the same sign and zero if otherwise. This equation pins the contact line if $\theta_D \in [\theta_R, \theta_A]$. If the contact line moves, it automatically picks the correct static contact angle: θ_A if the contact line advances and θ_R if the contact line recedes. It should be noted that, at the leading order, (3.3) is consistent with equation (6) in Prabhala, Panchagnula & Vedantam (2013) for quasi-static computations of drop shapes on hysteric surfaces.

This boundary condition is very easy to implement numerically. In each cell face on the solid wall, we compute the two copies of wall potentials, namely $L(\phi, \nabla\phi; \theta_A)$ and $L(\phi, \nabla\phi; \theta_R)$. Then we compare the cell average of these two potentials, and decide which one (including 0) we need to take into (3.3). There is no need to extract θ_D or contact line velocity.

3.2. *Energy law for contact angle hysteresis*

In thermodynamics hysteresis cannot be described by a path-independent state function. Therefore, we cannot find a single-valued wall energy to describe the contact line motion with CAH. However, that does not prevent the system from satisfying a dissipative energy law.

https://doi.org/10.1017/jfm.2020.465 Published online by Cambridge University Press

THEOREM 3.1. *The equation system* (2.7)–(2.10)*, together with the boundary conditions* (2.11)*,* (2.12)*,* (2.14) *and* (3.3)*, satisfies the energy law*

$$\frac{\mathrm{d}}{\mathrm{d}t}\left\{\int_{\Omega}\left(\frac{1}{2}\rho|\boldsymbol{u}|^2+f_m\right)\mathrm{d}\boldsymbol{x}+\int_{\partial\Omega_w}f_w(\phi;\theta_A)\,\mathrm{d}s\right\}=\mathcal{W}-\mathcal{D}-\mathcal{D}_{cah},\tag{3.5}$$

where

$$\mathcal{W}=\oint_{\partial\Omega}\boldsymbol{n}\cdot\boldsymbol{T}\cdot\boldsymbol{u}\,\mathrm{d}s+\int_{\Omega}\rho\boldsymbol{g}\cdot\boldsymbol{u}\,\mathrm{d}\boldsymbol{x}$$

is the power of the reversible work done by the boundary and body force,

$$\mathcal{D}=\int_{\Omega}\boldsymbol{\tau}:\nabla\boldsymbol{u}\,\mathrm{d}\boldsymbol{x}+\int_{\Omega}M|\nabla G|^2\,\mathrm{d}\boldsymbol{x}+\int_{\partial\Omega_w}\Gamma\tilde{L}^2\,\mathrm{d}s\geq 0$$

is the dissipation rate as seen in the standard contact line problem, and

$$\mathcal{D}_{cah}=\int_{\partial\Omega_w}[f_w'(\phi;\theta_R)-f_w'(\phi;\theta_A)]\min\left(\frac{\mathrm{D}\phi}{\mathrm{D}t},0\right)\mathrm{d}s\geq 0$$

is the dissipation rate due to CAH. Here $\boldsymbol{T}=-p\boldsymbol{I}+\boldsymbol{\tau}+\boldsymbol{\tau}_\phi$ *is the total stress and* $\boldsymbol{\tau}_\phi$ *is given by* (B 7)*. The term in the curly braces is the 'free energy' including the kinetic energy, the mixing energy and the wall energy based on the advancing contact angle.*

Proof. To save space, we will focus on the proof related to CAH and only provide a sketch for the rest.

From (2.9), (2.16) and (2.17), we recover

$$\frac{\mathrm{D}\rho}{\mathrm{D}t}=\frac{\rho_1-\rho_2}{2}\frac{\mathrm{D}\phi}{\mathrm{D}t}=\frac{\rho_1-\rho_2}{2}\nabla\cdot(M\nabla G)=-\nabla\cdot\boldsymbol{J}.\tag{3.6}$$

By taking the inner product of (2.7) and $\boldsymbol{u}$, taking the inner product of (3.6) and $|\boldsymbol{u}|^2/2$, and summing them up, we obtain

$$\frac{\mathrm{d}}{\mathrm{d}t}\int_{\Omega}\frac{1}{2}\rho|\boldsymbol{u}|^2\,\mathrm{d}\boldsymbol{x}=\oint_{\partial\Omega}\boldsymbol{n}\cdot\boldsymbol{T}\cdot\boldsymbol{u}\,\mathrm{d}s+\int_{\Omega}\rho\boldsymbol{g}\cdot\boldsymbol{u}\,\mathrm{d}\boldsymbol{x}-\int_{\Omega}\boldsymbol{T}:\nabla\boldsymbol{u}\,\mathrm{d}\boldsymbol{x}.\tag{3.7}$$

Here we have used the incompressibility condition (2.8) and replaced $G\nabla\phi$ with $\nabla\cdot\boldsymbol{\tau}_\phi$ based on the identity (B 19). The derivation of this equation is essentially the same as (C 6). The only difference is that we now include a body force and replace $\tilde{\boldsymbol{T}}$ with $\boldsymbol{T}$.

By taking the inner product of (2.9) and G, taking the inner product of (2.10) with $-\mathrm{D}\phi/\mathrm{D}t$, and summing them up, we obtain

$$\frac{\mathrm{d}}{\mathrm{d}t}\int_{\Omega}f_m\,\mathrm{d}\boldsymbol{x}=\int_{\partial\Omega_w}\lambda\boldsymbol{n}\cdot\nabla\phi\frac{\mathrm{D}\phi}{\mathrm{D}t}\,\mathrm{d}s+\int_{\Omega}\boldsymbol{\tau}_\phi:\nabla\boldsymbol{u}\,\mathrm{d}\boldsymbol{x}-\int_{\Omega}M|\nabla\phi|^2\,\mathrm{d}\boldsymbol{x},\tag{3.8}$$

where we have considered (2.14). The proof of this equation is essentially the reverse of (B 5).

The $\tilde{L}$ term in (3.3) takes different values depending on the state of the contact line. If the contact line advances, we have $\mathrm{D}\phi/\mathrm{D}t=\partial\phi/\partial t+\boldsymbol{u}_w\cdot\nabla\phi>0$ and $\tilde{L}=L_A=\lambda\boldsymbol{n}\cdot\nabla\phi+f_w'(\phi;\theta_A)$ on $\partial\Omega_w$; if the contact line recedes, we have $\mathrm{D}\phi/\mathrm{D}t<0$ and $\tilde{L}=L_R=$

https://doi.org/10.1017/jfm.2020.465 Published online by Cambridge University Press

$\lambda \boldsymbol{n}\cdot\nabla\phi + f_w'(\phi;\theta_R)$; if the contact line is pinned, we have $\mathrm{D}\phi/\mathrm{D}t = 0$ and $\tilde{L} = 0$. This leads to the identity

$$\begin{aligned}\tilde{L}\frac{\mathrm{D}\phi}{\mathrm{D}t} &= \lambda\boldsymbol{n}\cdot\nabla\phi\frac{\mathrm{D}\phi}{\mathrm{D}t} + f_w'(\phi;\theta_A)\max\left(\frac{\mathrm{D}\phi}{\mathrm{D}t},0\right) + f_w'(\phi;\theta_R)\min\left(\frac{\mathrm{D}\phi}{\mathrm{D}t},0\right)\\ &= \left[\lambda\boldsymbol{n}\cdot\nabla\phi + f_w'(\phi;\theta_A)\right]\frac{\mathrm{D}\phi}{\mathrm{D}t} + \left[f_w'(\phi;\theta_R) - f_w'(\phi;\theta_A)\right]\min\left(\frac{\mathrm{D}\phi}{\mathrm{D}t},0\right). \end{aligned} \tag{3.9}$$

By taking the inner product of (3.3) and $-(1/\Gamma)(\mathrm{D}\phi/\mathrm{D}t)$ on $\partial\Omega_w$, and considering (3.9), we obtain

$$\begin{aligned}&\int_{\partial\Omega_w} -\frac{1}{\Gamma}\left(\frac{\mathrm{D}\phi}{\mathrm{D}t}\right)^2 \mathrm{d}s\\ &\quad= \int_{\partial\Omega_w}\left\{\left[\lambda\boldsymbol{n}\cdot\nabla\phi + f_w'(\phi;\theta_A)\right]\frac{\mathrm{D}\phi}{\mathrm{D}t} + \left[f_w'(\phi;\theta_R) - f_w'(\phi;\theta_A)\right]\min\left(\frac{\mathrm{D}\phi}{\mathrm{D}t},0\right)\right\}\mathrm{d}s\\ &\quad= \int_{\partial\Omega_w}\lambda\boldsymbol{n}\cdot\nabla\phi\frac{\mathrm{D}\phi}{\mathrm{D}t}\,\mathrm{d}s + \frac{\mathrm{d}}{\mathrm{d}t}\int_{\partial\Omega_w} f_w(\phi;\theta_A)\,\mathrm{d}s\\ &\qquad+ \int_{\partial\Omega_w}\left[f_w'(\phi;\theta_R) - f_w'(\phi;\theta_A)\right]\min\left(\frac{\mathrm{D}\phi}{\mathrm{D}t},0\right)\mathrm{d}s. \end{aligned} \tag{3.10}$$

Equation (3.5) can be easily obtained by combining (3.7), (3.8) and (3.10).

The positivity of $\mathcal{D}$ is easily seen. Since $\theta_A > \theta_R$, we have $f_w'(\phi;\theta_A) > f_w'(\phi;\theta_R)$ based on (3.2). Thus, both $f_w'(\phi;\theta_R) - f_w'(\phi;\theta_A)$ and $\min(\mathrm{D}\phi/\mathrm{D}t, 0)$ are non-positive, and $\mathcal{D} \geq 0$ follows. □

Remark 3.1. This theorem neither assumes the fluid domain Ω to be fixed, nor does it require $\boldsymbol{n}\cdot\boldsymbol{u} = 0$ on the boundary. It should be noted that (3.5) can also be cast into

$$\frac{\mathrm{d}}{\mathrm{d}t}\left\{\int_\Omega\left(\frac{1}{2}\rho|\boldsymbol{u}|^2 + f_m\right)\mathrm{d}\boldsymbol{x} + \int_{\partial\Omega_w} f_w(\phi;\theta_R)\,\mathrm{d}s\right\} = \mathcal{W} - \mathcal{D} - \tilde{\mathcal{D}}_{cah}, \tag{3.11}$$

with

$$\tilde{\mathcal{D}}_{cah} = \int_{\partial\Omega_w}\left[f_w'(\phi;\theta_A) - f_w'(\phi;\theta_R)\right]\max\left(\frac{\mathrm{D}\phi}{\mathrm{D}t},0\right)\mathrm{d}s \geq 0.$$

It is obvious that $\mathcal{D}_{cah} = 0$ if the contact line never recedes and $\tilde{\mathcal{D}}_{cah} = 0$ if the contact line never advances. The dissipation of CAH takes action only when a region on the solid surface is swept by both an advancing contact line and a receding contact line.

It should be noted that the 'free energy' in (3.5) can not be understood in the traditional sense. Not all this 'free energy' can be used to do work and the portion that can do work is path dependent. For example, if we use θ_A to define the wall energy then all the 'free energy' can do work if the contact line advances; but if the contact line recedes, only part of the 'free energy' can do work and the missing part is $\mathcal{D}_{cah}$. Similarly, if we use θ_R then only part of the 'free energy' can do work when the contact line advances and the missing part is $\tilde{\mathcal{D}}_{cah}$.

In the following we provide a physical explanation to the dissipation terms that occur on the solid wall. We consider a contact line problem in two dimensions with a stationary

https://doi.org/10.1017/jfm.2020.465 Published online by Cambridge University Press

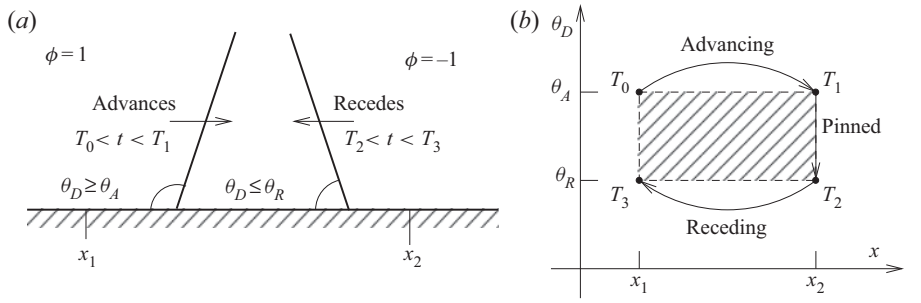


FIGURE 2. Dissipations due to contact line motion. The contact line advances from x_1 to x_2 and then recedes back to x_1. (*a*) Advancing and receding motions of a contact line. (*b*) Hysteresis loop in the x–θ_D plane.

solid wall (such that $\mathrm{D}\phi/\mathrm{D}t = \partial\phi/\partial t$) for simplicity. Suppose a contact line advances over a region $A = [x_1, x_2]$ with length $a = x_2 - x_1$ on the solid wall at $t \in [T_0, T_3]$, as illustrated in figure 2. At $t = T_0$, the contact line starts from x_1 with $\theta_D = \theta_A$. Then the contact line advances with $\theta_D \geq \theta_A$ and arrives at x_1 at $t = T_1$. During $[T_1, T_2]$ the contact line is pinned at x_2 and adjusts its microscopic contact angle from θ_A to θ_R. Then the contact line recedes with $\theta_D \leq \theta_R$ and returns to its original position x_1 at $t = T_3$.

In the phase-field context, we have $\phi = -1$ at $t = T_0$, $\phi = 1$ at $t \in [T_1, T_2]$ and $\phi = -1$ again at $t = T_3$ in A. Correspondingly, $\partial\phi/\partial t \geq 0$ at $t \in [T_0, T_1]$, $\partial\phi/\partial t = 0$ at $t \in [T_1, T_2]$ and $\partial\phi/\partial t \leq 0$ at $t \in [T_2, T_3]$. Then the energy dissipated due to CAH is

$$\begin{aligned}\int_{T_0}^{T_3} \mathcal{D}_{cah}\,\mathrm{d}t &= \int_{T_0}^{T_3}\int_A [f_w'(\phi;\theta_R) - f_w'(\phi;\theta_A)]\min\left(\frac{\partial\phi}{\partial t}, 0\right)\mathrm{d}s\,\mathrm{d}t \\ &= \int_A\int_{T_2}^{T_3} [f_w'(\phi;\theta_R) - f_w'(\phi;\theta_A)]\frac{\partial\phi}{\partial t}\,\mathrm{d}t\,\mathrm{d}s \\ &= \int_A\int_{\phi=1}^{\phi=-1} [f_w'(\phi;\theta_R) - f_w'(\phi;\theta_A)]\,\mathrm{d}\phi\,\mathrm{d}s \\ &= \int_A \left[f_w(\phi;\theta_R)|_{\phi=1}^{\phi=-1} - f_w(\phi;\theta_A)|_{\phi=1}^{\phi=-1}\right]\mathrm{d}s \\ &= \sigma(\cos\theta_R - \cos\theta_A)a, \end{aligned} \tag{3.12}$$

which is non-negative because $\theta_R \leq \theta_A$. This corresponds to the region enclosed by $x = x_1$, $x = x_2$, $\theta_D = \theta_A$ and $\theta_D = \theta_R$, which is shaded in figure 2(*b*). The same amount of dissipation can also be obtained using $\mathcal{D}_{cah}^*$.

Meanwhile, during $[T_0, T_1]$, the dissipation due to the deviation of θ_D from θ_A is

$$\begin{aligned}\int_{T_0}^{T_1}\int_A \Gamma\tilde{L}^2\,\mathrm{d}s\,\mathrm{d}t &= \int_{T_0}^{T_1}\int_A \Gamma L_A^2\,\mathrm{d}s\,\mathrm{d}t = \int_A\int_{T_0}^{T_1} -L_A\frac{\partial\phi}{\partial t}\,\mathrm{d}t\,\mathrm{d}s \\ &= \int_A\int_{T_0}^{T_1} (f_w'(\phi;\theta_D) - f_w'(\phi;\theta_A))\frac{\partial\phi}{\partial t}\,\mathrm{d}t\,\mathrm{d}s\end{aligned}$$

https://doi.org/10.1017/jfm.2020.465 Published online by Cambridge University Press

$$= \int_A \left[f_w(\phi; \theta_D)|_{\phi=-1}^{\phi=1} - f_w(\phi; \theta_A)|_{\phi=-1}^{\phi=1} \right] \mathrm{d}s$$
$$= \sigma(\cos\theta_A - \cos\theta_D)a, \tag{3.13}$$

where we have used the relation $\lambda \boldsymbol{n} \cdot \nabla\phi = -f_w'(\phi; \theta_D)$ (see (A 7)) in the third equality. This corresponds to the region enclosed by the advancing branch of θ_D and $\theta_D = \theta_A$ in figure 2(*b*). It should be noted a tangential force of $\sigma\cos\theta_D$ has to be exerted at the contact line in order to move the interface with a contact angle θ_D while the wettability supplies a force of $\sigma\cos\theta_A$. The difference between these two forces, which has been referred to as the uncompensated (Qian *et al.* 2003) or unbalanced (Ren & E 2007) Young's stress in the literature, is responsible for the additional dissipation in (3.13). Similarly, we can get the dissipation due to the deviation of θ_D from θ_R during $[T_2, T_3]$, i.e.

$$\int_{T_2}^{T_3} \int_A \Gamma \tilde{L}^2 \,\mathrm{d}s\,\mathrm{d}t = \sigma(\cos\theta_D - \cos\theta_R)a, \tag{3.14}$$

which corresponds to the region enclosed by $\theta_D = \theta_R$ and the receding branch of θ_D. A complete hysteresis loop is formed if the contact line stays pinned at x_1 at $t \geq T_3$ and θ_D changes from θ_R to θ_A. This pinned state does not cause any dissipation on the solid wall (of course, viscous dissipation in the bulk may be incurred to deform the interface away from the contact line). The argument here can be easily extended to three-dimensional (3-D) flows, where A is a two-dimensional (2-D) region on the wall boundary and a is the area of A.

4. Numerical discretization

4.1. *Weak form and discrete energy law*

The weak form of the governing equations (2.7)–(2.10) and (3.3) can be expressed as

$$\left(\rho\frac{D\boldsymbol{u}}{Dt} + \boldsymbol{J}\cdot\nabla\boldsymbol{u}, \hat{\boldsymbol{u}}\right) = \left(\boldsymbol{n}\cdot(-p\boldsymbol{I}+\boldsymbol{\tau}), \hat{\boldsymbol{u}}\right)_{\partial\Omega} - \left(-p\boldsymbol{I}+\boldsymbol{\tau}, \nabla\hat{\boldsymbol{u}}\right) + (G\nabla\phi + \rho\boldsymbol{g}, \hat{\boldsymbol{u}}), \tag{4.1}$$

$$-\left(\nabla\cdot\boldsymbol{u}, \hat{p}\right) = 0, \tag{4.2}$$

$$\left(\frac{\mathrm{D}\phi}{\mathrm{D}t}, \hat{\phi}\right) = \left(M\nabla G, \nabla\hat{\phi}\right), \tag{4.3}$$

$$\left(G, \hat{G}\right) - \frac{1}{\Gamma}\left(\frac{\mathrm{D}\phi}{\mathrm{D}t}, \hat{G}\right)_{\partial\Omega_w} = (\lambda\nabla\phi, \nabla\hat{G}) + (\lambda f_0'(\phi), \hat{G}) + \left(A, \hat{G}\right)_{\partial\Omega_w}, \tag{4.4}$$

where $(\cdot,\cdot)$ denotes the L_2 inner product in the domain Ω, $(\cdot,\cdot)_{\partial\Omega}$ and $(\cdot,\cdot)_{\partial\Omega_w}$ denote the inner product on $\partial\Omega$ and $\partial\Omega_w$. We seek solutions $\boldsymbol{u} \in H^1(\Omega)^d$, $p \in L^2(\Omega)$, $\phi \in H^1(\Omega)$ and $G \in H^1(\Omega)$ satisfying the equations above, where d is the dimension of the problem. The variables with $\hat{}$ are the corresponding test functions. The special form of (4.4) is motivated by the proof of Theorem 3.1. The $\lambda\boldsymbol{n}\cdot\nabla\phi$ term in $\tilde{L}$ is cancelled out on $\partial\Omega_w$

https://doi.org/10.1017/jfm.2020.465 Published online by Cambridge University Press

unless the contact line is pinned. The term A comes from CAH and can be expressed as

$$A = \begin{cases} f_w'(\phi;\theta_A) = -\frac{3}{4}\sigma\cos\theta_A(1-\phi^2) & \text{if } 0 \geq L_A \geq L_R \text{ (contact line advances)}, \\ f_w'(\phi;\theta_R) = -\frac{3}{4}\sigma\cos\theta_R(1-\phi^2) & \text{if } L_A \geq L_R > 0 \text{ (contact line recedes)}, \\ -\lambda \boldsymbol{n}\cdot\nabla\phi & \text{otherwise.} \end{cases} \tag{4.5}$$

If $\nabla\cdot\boldsymbol{u} = 0$ is satisfied in the strong sense then the energy law (3.5) is recovered if we take $\hat{\boldsymbol{u}} = \boldsymbol{u}$, $\hat{\phi} = G$ and $\hat{G} = \mathrm{D}\phi/\mathrm{D}t$. To obtain a similar energy law under the weak incompressibility condition (4.2), special care must be taken on the momentum equation, e.g. the skew-symmetric form for flows with constant density and the method of Guermond & Quartapelle (2000) for flows with variable density.

There have been energy stable numerical schemes for moving contact line problems with variable densities (e.g. Gao & Wang 2014; Yu & Yang 2017; Metzger 2019). But they are all first order in time and the time step has to be very small for reasonable temporal accuracy. In this work we adopt a second-order time discretization based on the Crank–Nicolson method and a skew-symmetric form for the convection term in the momentum equation. In the semi-discrete form, we seek $\boldsymbol{u}^{n+1}$, $p^{n+1/2}$, ϕ^{n+1} and $G^{n+1/2}$ satisfying

$$\begin{aligned} &\left(\rho^{n+1/2}\left(\frac{\boldsymbol{u}^{n+1}-\boldsymbol{u}^n}{\Delta t} + \bar{\boldsymbol{u}}^{n+1/2}\cdot\nabla\boldsymbol{u}^{n+1/2} + \frac{1}{2}(\nabla\cdot\bar{\boldsymbol{u}}^{n+1/2})\boldsymbol{u}^{n+1/2}\right), \hat{\boldsymbol{u}}\right) \\ &\quad - \left(\frac{\rho_1-\rho_2}{2}M\nabla G^{n+1/2}\cdot\nabla\boldsymbol{u}^{n+1/2}, \hat{\boldsymbol{u}}\right) \\ &\qquad = \left(p^{n+1/2}\boldsymbol{I} - \mu^{n+1/2}\boldsymbol{E}(\boldsymbol{u}^{n+1/2}), \nabla\hat{\boldsymbol{u}}\right) + \left(G^{n+1/2}\nabla\phi^{n+1/2}, \hat{\boldsymbol{u}}\right), \end{aligned} \tag{4.6}$$

$$-\left(\nabla\cdot\boldsymbol{u}^n, \hat{p}\right) = 0, \tag{4.7}$$

$$\left(\frac{\phi^{n+1}-\phi^n}{\Delta t} + \boldsymbol{u}^{n+1/2}\cdot\nabla\phi^{n+1/2}, \hat{\phi}\right) = (-M\nabla G^{n+1/2}, \nabla\hat{\phi}), \tag{4.8}$$

$$\begin{aligned} &(G^{n+1/2}, \hat{G}) - \left(\frac{1}{\Gamma}\left(\frac{\phi^{n+1}-\phi^n}{\Delta t} + \boldsymbol{u}_w\cdot\nabla\phi^{n+1/2}\right), \hat{G}\right)_{\partial\Omega_w} \\ &\qquad = \left(\lambda\nabla\phi^{n+1/2}, \nabla\hat{G}\right) + \left(\lambda Df_0(\phi^n, \phi^{n+1}), \hat{G}\right) + \sum_{e\in\mathcal{T}(\partial\Omega_w)}\left(A^{n+1/2}, \hat{G}\right)_e, \end{aligned} \tag{4.9}$$

for all admissible test functions $\hat{\boldsymbol{u}}$, $\hat{p}$, $\hat{\phi}$ and $\hat{G}$. Here, $\Delta t = t^{n+1} - t^n$ is the time step, $\boldsymbol{u}^{n+1/2} = (\boldsymbol{u}^{n+1} + \boldsymbol{u}^n)/2$ and $\phi^{n+1/2} = (\phi^{n+1} + \phi^n)/2$ are second-order approximations at half-time level $t^{n+1/2}$, $\bar{\boldsymbol{u}}^{n+1/2} = (3\boldsymbol{u}^n - \boldsymbol{u}^{n-1})/2$ ($\bar{\boldsymbol{u}}^{n+1/2} = \boldsymbol{u}^n$ for $n = 0$) is an explicit approximation at $t^{n+1/2}$ by extrapolation,

$$\rho^{n+1/2} = \frac{1+\phi^{n+1/2}}{2}\rho_1 + \frac{1-\phi^{n+1/2}}{2}\rho_2, \quad \mu^{n+1/2} = \frac{1+\phi^{n+1/2}}{2}\mu_1 + \frac{1-\phi^{n+1/2}}{2}\mu_2,$$

$\mathcal{T}(\partial\Omega_w)$ denotes the triangulation of the wall boundary $\partial\Omega_w$ and e denotes an element face (or edge in two dimensions) on $\partial\Omega_w$. We have also introduced the strain rate tensor

https://doi.org/10.1017/jfm.2020.465 Published online by Cambridge University Press

$\boldsymbol{E}(\boldsymbol{u}) = \nabla\boldsymbol{u} + (\nabla\boldsymbol{u})^T$ for convenience. The term Df_0, first introduced by Du & Nicolaides (1991) and sometimes referred to as the discrete variational derivative (Gomez & van der Zee 2017), is a second-order approximation to $f_0'(\phi^{n+1/2})$ for the purpose of energy stability:

$$Df_0(\phi^n, \phi^{n+1}) = \begin{cases} \dfrac{f_0(\phi^{n+1}) - f_0(\phi^n)}{\phi^{n+1} - \phi^n} & \text{if } \phi^{n+1} \neq \phi^n, \\ f_0'(\phi^n) & \text{if } \phi^{n+1} = \phi^n. \end{cases} \tag{4.10}$$

The term $A^{n+1/2}$ takes care of CAH. For the convenience of numerical implementation, we determine the status of the contact line by comparing the integral of wall potential. On each element face e on the wall boundary, we have

$$A^{n+1/2} = \begin{cases} Df_w(\phi^n, \phi^{n+1}; \theta_A) & \text{if } 0 \geq L_A^* \geq L_R^*, \\ Df_w(\phi^n, \phi^{n+1}; \theta_R) & \text{if } L_A^* \geq L_R^* > 0, \\ -\lambda\boldsymbol{n}\cdot\nabla\phi^{n+1/2} & \text{otherwise}, \end{cases} \tag{4.11}$$

where Df_w is the discrete variational derivative of f_w. L_A^* and L_R^* are the integrals of wall potentials on the element face and they are defined explicitly for numerical convenience: $L_{A,R}^* = \int_e [\lambda\boldsymbol{n}\cdot\nabla\phi^n + f_w'(\phi^n; \theta_{A,R})]\,\mathrm{d}s$.

In most problems we impose either a zero traction condition $\boldsymbol{n}\cdot\boldsymbol{T} = \boldsymbol{0}$ or a Dirichlet condition for $\boldsymbol{u}$ on the domain boundary, which causes the surface integral term in (4.1) to vanish. Thus, for brevity, the surface integral term is dropped in (4.6).

This scheme does not have unconditional energy stability, but it satisfies the following discrete energy law for matched density.

THEOREM 4.1. *If $\rho_1 = \rho_2 = \rho$ and $\boldsymbol{u}_w = 0$, then the semi-discrete system (4.6)–(4.9) with the non-penetrating essential boundary condition $\boldsymbol{n}\cdot\boldsymbol{u}|_{\partial\Omega} = 0$ satisfies the discrete energy law*

$$\begin{aligned} \frac{\mathcal{F}_A^{n+1} - \mathcal{F}_A^n}{\Delta t} = &-\frac{1}{2}\left\|\sqrt{\mu^{n+1/2}}\boldsymbol{E}(\boldsymbol{u}^{n+1/2})\right\|^2 - \left\|\sqrt{M}\nabla G^{n+1/2}\right\|^2 \\ &- \left\|\frac{1}{\sqrt{\Gamma}}\frac{\phi^{n+1} - \phi^n}{\Delta t}\right\|_{\partial\Omega_w}^2 + \sum_{e\in\mathcal{T}(\partial\Omega_w)} B_e, \end{aligned} \tag{4.12}$$

where

$$\mathcal{F}_A^n = \int_\Omega \left[\frac{1}{2}\rho|\boldsymbol{u}^n|^2 + \lambda\left(\frac{1}{2}|\nabla\phi^n|^2 + f_0(\phi^n)\right)\right]\mathrm{d}\boldsymbol{x} + \int_{\partial\Omega_w} f_w(\phi^n; \theta_A)\,\mathrm{d}s \tag{4.13}$$

and

$$B_e = \begin{cases} 0 & \text{if } 0 \geq L_A^* \geq L_R^*, \\ \left(Df_w(\phi^n, \phi^{n+1}; \theta_A) - Df_w(\phi^n, \phi^{n+1}; \theta_R), \dfrac{\phi^{n+1} - \phi^n}{\Delta t}\right)_e & \text{if } L_A^* \geq L_R^* > 0, \\ \left(\lambda\boldsymbol{n}\cdot\nabla\phi^{n+1/2} + Df_w(\phi^n, \phi^{n+1}; \theta_A), \dfrac{\phi^{n+1} - \phi^n}{\Delta t}\right)_e & \text{otherwise}. \end{cases} \tag{4.14}$$

https://doi.org/10.1017/jfm.2020.465 Published online by Cambridge University Press

Proof. Taking $\hat{\boldsymbol{u}} = \boldsymbol{u}^{n+1/2}$, the left-hand side (LHS) of (4.6) becomes

$$\begin{aligned}\text{LHS} &= \left(\rho\frac{\boldsymbol{u}^{n+1}-\boldsymbol{u}^{n}}{\Delta t}, \frac{\boldsymbol{u}^{n+1}+\boldsymbol{u}^{n}}{2}\right)\\ &\quad + \left(\bar{\boldsymbol{u}}^{n+1/2}\cdot\nabla\boldsymbol{u}^{n+1/2} + \frac{1}{2}(\nabla\cdot\bar{\boldsymbol{u}}^{n+1/2})\boldsymbol{u}^{n+1/2}, \boldsymbol{u}^{n+1/2}\right)\\ &= \frac{\rho}{2\Delta t}\left(\|\boldsymbol{u}^{n+1}\|^2 - \|\boldsymbol{u}^{n}\|^2\right) + \frac{1}{2}\left(\nabla\cdot\left(\bar{\boldsymbol{u}}^{n+1/2}\left|\boldsymbol{u}^{n+1/2}\right|^2\right), 1\right)\\ &= \frac{\rho}{2\Delta t}\left(\|\boldsymbol{u}^{n+1}\|^2 - \|\boldsymbol{u}^{n}\|^2\right),\end{aligned} \tag{4.15}$$

where we have used the boundary condition $\bar{\boldsymbol{u}}^{n+1/2}\cdot\boldsymbol{n}|_{\partial\Omega} = (3\boldsymbol{u}^{n+1}-\boldsymbol{u}^{n})/2\cdot\boldsymbol{n}|_{\partial\Omega} = \boldsymbol{0}$ in the last equality. It should be noted that this equation does not require $\nabla\cdot\boldsymbol{u}^{n} = 0$ to be exactly satisfied. The right-hand side (RHS) of (4.6) becomes

$$\begin{aligned}\text{RHS} &= \left(p^{n+1/2}, \nabla\cdot\boldsymbol{u}^{n+1/2}\right) - \left(\mu^{n+1/2}\boldsymbol{E}(\boldsymbol{u}^{n+1/2}), \nabla\boldsymbol{u}^{n+1/2}\right) + \left(G^{n+1/2}\nabla\phi^{n+1/2}, \boldsymbol{u}^{n+1/2}\right)\\ &= \left(p^{n+1/2}, \nabla\cdot\boldsymbol{u}^{n+1/2}\right) - \|\sqrt{\mu^{n+1/2}}\boldsymbol{E}(\boldsymbol{u}^{n+1/2})\|^2 + \left(G^{n+1/2}\nabla\phi^{n+1/2}, \boldsymbol{u}^{n+1/2}\right).\end{aligned} \tag{4.16}$$

Since (4.7) is satisfied at each time level, it follows that $-(\nabla\cdot((\boldsymbol{u}^{n+1}+\boldsymbol{u}^{n})/2), \hat{p}) = 0$. By taking $\hat{p} = p^{n+1/2}$, we obtain

$$-\left(\nabla\cdot\boldsymbol{u}^{n+1/2}, p^{n+1/2}\right) = 0. \tag{4.17}$$

By taking $\hat{\phi} = G^{n+1/2}$, (4.8) leads to

$$\left(\frac{\phi^{n+1}-\phi^{n}}{\Delta t}, G^{n+1/2}\right) + \left(\boldsymbol{u}^{n+1/2}\cdot\nabla\phi^{n+1/2}, G^{n+1/2}\right) = -\left(M\nabla G^{n+1/2}, \nabla G^{n+1/2}\right). \tag{4.18}$$

We then take $\hat{G} = (\phi^{n+1}-\phi^{n})/\Delta t$ in (4.9) and obtain

$$\begin{aligned}&\left(G^{n+1/2}, \frac{\phi^{n+1}-\phi^{n}}{\Delta t}\right) - \left(\frac{1}{\Gamma}\frac{\phi^{n+1}-\phi^{n}}{\Delta t}, \frac{\phi^{n+1}-\phi^{n}}{\Delta t}\right)\\ &\quad= \left(\lambda\nabla\left(\frac{\phi^{n+1}+\phi^{n}}{2}\right), \nabla\left(\frac{\phi^{n+1}-\phi^{n}}{\Delta t}\right)\right) + \left(\lambda Df_0(\phi^{n}, \phi^{n+1}), \frac{\phi^{n+1}-\phi^{n}}{\Delta t}\right)\\ &\qquad+ \sum_{e\in\mathcal{T}(\partial\Omega_w)}\left(A^{n+1/2}, \frac{\phi^{n+1}-\phi^{n}}{\Delta t}\right)_e\\ &\quad= \left(\frac{\lambda}{2}\left(|\nabla\phi^{n+1}|^2 - |\nabla\phi^{n}|^2\right), \frac{1}{\Delta t}\right) + \left(\lambda\left(f_0(\phi^{n+1}) - f_0(\phi^{n})\right), \frac{1}{\Delta t}\right)\\ &\qquad+ \left(Df_w(\phi^{n}, \phi^{n+1}; \theta_A), \frac{\phi^{n+1}-\phi^{n}}{\Delta t}\right)_{\partial\Omega_w}\\ &\qquad+ \sum_{e\in\mathcal{T}(\partial\Omega_w)}\left(A^{n+1/2} - Df_w(\phi^{n}, \phi^{n+1}; \theta_A), \frac{\phi^{n+1}-\phi^{n}}{\Delta t}\right)_e\end{aligned}$$

https://doi.org/10.1017/jfm.2020.465 Published online by Cambridge University Press

$$= \frac{1}{\Delta t}\int_{\Omega}\left[\left(\frac{1}{2}\lambda|\nabla\phi^{n+1}|^2 + \lambda f_0(\phi^{n+1})\right) - \left(\frac{1}{2}\lambda|\nabla\phi^{n}|^2 + \lambda f_0(\phi^{n})\right)\right]\mathrm{d}\boldsymbol{x}$$
$$+ \frac{1}{\Delta t}\int_{\partial\Omega_w}\left[f_w(\phi^{n+1};\theta_A) - f_w(\phi^{n};\theta_A)\right]\mathrm{d}s - \sum_{e\in\mathcal{T}(\partial\Omega_w)} B_e. \tag{4.19}$$

Finally, by summing up equations (4.15)–(4.18) and subtracting (4.19), we arrive at (4.12). □

Remark 4.1. Since the proof is based on weak form and integration by parts, it can be easily extended to Galerkin methods with finite-dimensional function spaces (Shen *et al.* 2015). This energy law thus also applies to the fully discrete Galerkin finite element methods. The only additional requirement is that ϕ and G must share the same function space such that we can take $\hat{\phi} = G^{n+1/2}$ and $\hat{G} = (\phi^{n+1} - \phi^n)/\Delta t$.

Remark 4.2. The energy law (4.12) is dissipative except for the B_e term due to hystersis. We cannot prove this term to be non-positive from the weak form. However, we can show $B_e \leq 0$ if the strong form (3.3) is satisfied.

(i) If $0 > L_A^* > L_R^*$, the contact line advances and we have the trivial relation $B_e = 0$.
(ii) If $L_A^* > L_R^* > 0$, the contact line recedes according to the strong form (3.3) and, thus, $\phi^{n+1} - \phi^n \leq 0$. Similar to the inequality $f_w'(\phi,\theta_A) \geq f_w'(\phi;\theta_R)$, it can be easily shown that $Df_w(\phi^n,\phi^{n+1};\theta_A) \geq Df_w(\phi^n,\phi^{n+1};\theta_R)$ for $\phi^n, \phi^{n+1} \in [-1,1]$. Thus, we have $B_e \leq 0$ when the contact line recedes. This corresponds to the dissipation term $\mathcal{D}_{cah}$ in Theorem 3.1.
(iii) Otherwise, the contact line is pinned according to (3.3). In this case $\phi^{n+1} = \phi^n$ and, thus, $B_e = 0$.

It should be noted, however, that the weak form cannot exactly guarantee $\phi^{n+1} > \phi^n$ when $L_A^* > L_R^* > 0$ or $\phi^{n+1} = \phi^n$ when $L_A^* \geq 0 \geq L_R^*$. Thus, there might be regions with $Be > 0$ on wall boundaries in finite element computations. But, in practice, we do expect the weak solution to be a reasonable approximation to the strong solution and thus $B_e \leq 0$ to be 'approximately' satisfied.

Remark 4.3. In the absence of CAH, we have $\theta_A = \theta_R$ and, thus, $B_e = 0$. In this case, (4.12) recovers unconditional energy stability. It should be noted, however, that our numerical scheme is nonlinear and requires iterations. Thus, the time step still cannot be too large in practical computations.

Although we can not establish the energy stability for variable density problems, it does not raise severe stability concerns in practical computations as demonstrated later in § 5.3.

4.2. *Numerical methods*

The equation system (4.6)–(4.9) are solved by the finite element method using the deal.ii library (Bangerth, Hartmann & Kanschat 2007; Alzetta *et al.* 2018). Hierarchical adaptive meshes, quadrilateral in two dimensions and hexagonal in three dimensions, are used to discretize the computational domain. We use $Q2$ elements for $\boldsymbol{u}$, $Q1$ elements for p and $Q3$ elements for ϕ and G. For easy implementation, we solve the flow equations (4.6) and (4.7) separately from the Cahn–Hilliard equations (4.8) and (4.9), and then couple them together using a Picard iteration.

https://doi.org/10.1017/jfm.2020.465 Published online by Cambridge University Press

The nonlinear system of (4.8) and (4.9) are solved by Newton's method. On each element face e on $\partial\Omega_w$, we compute two copies of chemical potential L_A and L_R, and their integrals L_A^* and L_R^* on e. The value of $A^{n+1/2}$ is then determined from (4.11). The linear system in each Newton step is solved by the generalized minimal residual method (GMRES) with the incomplete LU factorization (ILU) preconditioner.

The momentum equation (4.6) and the continuity equation (4.7) are solved by the mixed finite element method. Thanks to the explicit $\bar{\boldsymbol{u}}^{n+1/2}$, we have the linear saddle point system

$$\begin{bmatrix} A & B^T \\ B & 0 \end{bmatrix} \begin{bmatrix} U \\ P \end{bmatrix} = \begin{bmatrix} F \\ 0 \end{bmatrix}, \tag{4.20}$$

where U and P are solutions vectors for $\boldsymbol{u}^{n+1}$ and $p^{n+1/2}$, respectively. The asymmetric block A comes from the momentum equation except for the pressure term and the block B comes from the continuity equation. For 2-D problems, where the number of degrees of freedom is typically below one million, we solve this system by the direct sparse linear solver UMFPACK (Davis 2004). For 3-D problems, we adopt the grad-div stabilization and solve the saddle point system by GMRES with a block-triangular Schur complement preconditioner developed by Heister & Rapin (2013). Detailed implementation of this preconditioner can be found in tutorial step-57 of deal.ii.

The solution procedure can be summarized as follows.

(i) Create an initial mesh which is refined at the interface and set the initial data $\boldsymbol{u}^0$ and ϕ^0.

(ii) For each time step $n \geq 0$, choose a proper Δt and perform the following steps until the stopping time is reached.

  (a) Based on ϕ^n, locally refine or coarsen the mesh such that the mesh is the finest at the interface with $h_{min} \in [0.5\epsilon, \epsilon]$ and gets coarsened away from the interface. Transfer data from the old mesh to the new mesh if the mesh is modified.

  (b) Let k denote the iteration step. Set $k = 0$ and $\boldsymbol{u}^{n+1/2,0} = \bar{\boldsymbol{u}}^{n+1/2}$, and iterate over the following steps until convergence.

    (1) Solve the Cahn–Hilliard equations (4.8) and (4.9) for $\phi^{n+1,k+1}$ and $G^{n+1/2,k+1}$ based on ϕ^n and $\boldsymbol{u}^{n+1/2,k}$.

    (2) Solve the flow equations (4.6) and (4.7) for $\boldsymbol{u}^{n+1,k+1}$ and $p^{n+1/2,k+1}$ based on $\boldsymbol{u}^n$, $\bar{\boldsymbol{u}}^{n+1/2}$, $\phi^{n+1/2,k+1}$ and $G^{n+1/2,k+1}$.

    (3) Set $k = k + 1$.

  (c) Update solution at t^{n+1}: $\boldsymbol{u}^{n+1} = \boldsymbol{u}^{n+1,k}$, $p^{n+1/2} = p^{n+1/2,k}$, $\phi^{n+1} = \phi^{n+1,k}$ and $G^{n+1/2} = G^{nh,k}$.

In practice we only need a few iterations in (ii*b*). For the computationally expensive 3-D problems, we only compute two iterations, i.e. up to $k = 2$.

5. Results and discussions

5.1. *Drop deformation in plane Poiseuille flow*

We first validate our method by computing the drop deformation with pinned contact lines in plane Poiseuille flow (Schleizer & Bonnecaze 1999). This 2-D test case has been widely used for validation purpose (e.g. Spelt 2005; Dupont & Legendre 2010; Huang *et al.* 2014; Liu *et al.* 2015). The computational domain is a $8H \times 2H$ rectangle with a drop adhered to the lower wall, as shown in figure 3(*a*). At the inlet, we impose a fully developed flow velocity $u = [1 - (y/H)^2]V_{max}$, where V_{max} is the maximum velocity along the centreline

https://doi.org/10.1017/jfm.2020.465 Published online by Cambridge University Press

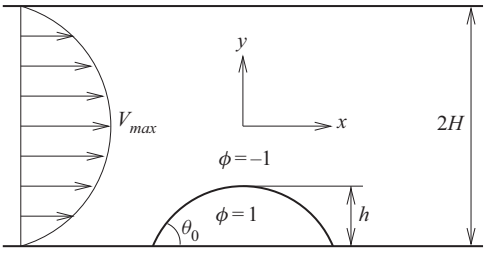


FIGURE 3. Schematic of a drop under shear in plane Poiseuille flow.

of the channel. At the outlet, we impose the zero traction condition. The lower and upper boundaries are stationary walls, where the velocity is set to zero. A drop is placed on the lower wall. Initially, the drop is a circular segment with contact angle $\theta_0 = 60^\circ$. The drop has radius $R_0 = 0.9023H$ and height $h = 0.4511H$, such that its area is $0.5H^2$. Inertia is neglected and the viscosity ratio is unity, i.e. $\mu_1 = \mu_2 = \mu$. Following Schleizer & Bonnecaze (1999), we define the characteristic shear rate $E = \partial u/\partial y|_{y=-H} = 2V_{max}/H$ and the capillary number $Ca = \mu Eh/\sigma = (\mu V_{max}/\sigma)(2h/H)$. To pin the contact line, we set $\theta_A = 170^\circ$ and $\theta_R = 10^\circ$.

For the Cahn–Hilliard equation, we introduce the following dimensionless parameters (Yue *et al.* 2010; Yue & Feng 2011): the Cahn number

$$Cn = \frac{\epsilon}{H} \tag{5.1}$$

that characterizes the thickness of the interface,

$$S = \frac{l_D}{H} = \frac{\sqrt{M\mu}}{H} \tag{5.2}$$

that characterizes the slip due to Cahn–Hilliard diffusion, and

$$\Pi = \frac{1}{\mu\Gamma H} \tag{5.3}$$

that characterizes the wall energy relaxation rate. Here $l_D = \sqrt{M\mu}$ is the diffusion length in the phase-field method, which is the counterpart of slip length in the slip models. For this test case, we choose $Cn = 0.01$, $S = 0.01$ and $\Pi = 0.1$. The computational mesh is adaptively refined at the interface and the mesh sizes are $h_{min} = H/128$ at the interface and $h_{max} = H/8$ in the bulk phases, as shown in figure 4(*a*). There are typically five layers of mesh cells in the diffuse interface (between $\phi = \pm 0.9$ contours), which guarantees the sufficient resolution of the interface (Yue *et al.* 2004, 2006). Thanks to the adaptive mesh refinement, there are only 3022 elements in the whole computational mesh corresponding to figure 4(*a*).

We take $\Delta t = 0.04(\mu H/\sigma)$ and run the simulation for 1000 steps, which is sufficient for the flow to reach steady state. The numerical results are given in figure 4. For different capillary numbers, the $\phi = 0$ level sets match the boundary integral curves very well. In theory, the contact lines should be pinned at $x/H = \pm 0.7814$. The contact line at the right is pinned very accurately for all Ca. In comparison, there is an observable error at the left contact line for $Ca = 0.15$: the intersection of $\phi = 0$ and the wall is shifted slightly downstream. This is because the contact angle is very small and the diffuse interface has a much larger intersection with the wall. This, in return, introduces more uncertainty to the exact location of the sharp interface.

https://doi.org/10.1017/jfm.2020.465 Published online by Cambridge University Press

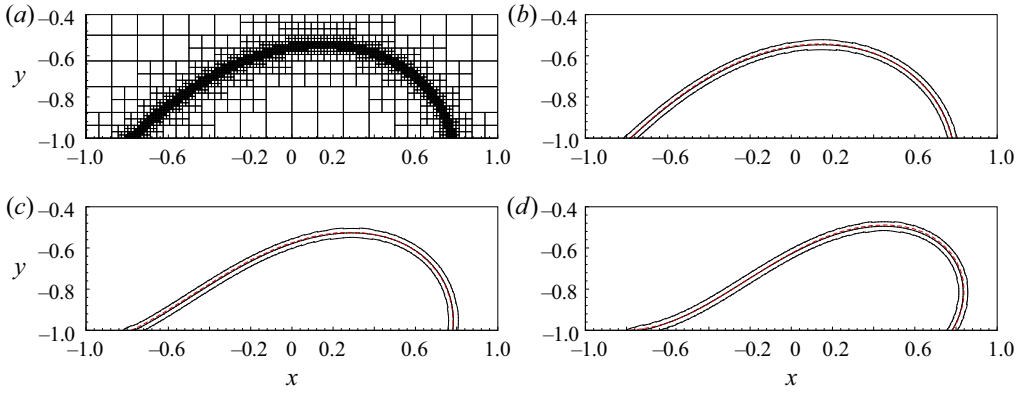


FIGURE 4. An example of the computational mesh near the drop (*a*) and steady-state drop shapes (*b–d*). The (red) dashed curve denotes the interface obtained by Schleizer & Bonnecaze (1999) using a boundary integral method. The (black) solid curves denote the $\phi = -0.9, 0, 0.9$ contours by the phase-field method. Computational mesh for (*a*) $Ca = 0.05$, (*b*) $Ca = 0.05$, (*c*) $Ca = 0.10$, (*d*) $Ca = 0.15$.

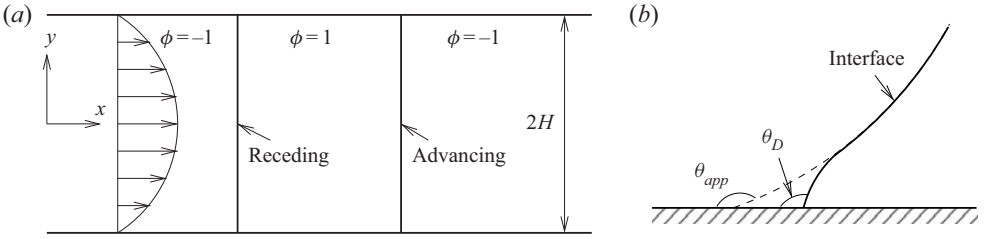


FIGURE 5. Schematic of advancing and receding interfaces under plane Poiseuille flow (*a*) and a zoomed-in view of the contact line (*b*). The dashed line in (*b*) represents a circular fit to the deformed interface.

5.2. *Advancing and receding interfaces in plane Poiseuille flow*

The contact lines in the previous section are pinned. In this subsection we investigate the dynamics of moving contact lines. We consider the advancing and receding interfaces between two parallel plates, as shown in figure 5(*a*). The velocity and stress boundary conditions are the same as those in the previous subsection. The domain size is $10H \times 2H$. The interfaces are initially vertical lines located at $x = 3H$ and $6H$. For convenience, we refer to the contact line on the left as the receding contact line and the one on the right as the advancing contact line, although they may both get pinned.

We still neglect inertia and only consider matched viscosities. At steady state, the interfaces together with the contact lines move at the average velocity $\bar{V} = \frac{2}{3}V_{max}$ of the Poiseuille flow. We thus define the capillary number as $Ca = \mu\bar{V}/\sigma$. In the following computations, we take $S = 0.01$, $\theta_A = 135^\circ$ and $\theta_R = 75^\circ$. Other parameters will be given in the detailed discussions.

The apparent contact angle is usually introduced to describe the macroscopic behaviour of the interface and there is never a unified definition that works for all flow conditions. In this work, following Hoffman (1975), we compute a circular fit to the $\phi = 0$ level set, and then determine θ_{app} based on the intersection between the circular fit and the wall, as shown in figure 5(*b*). At small capillary numbers, the interface away from the contact line

https://doi.org/10.1017/jfm.2020.465 Published online by Cambridge University Press

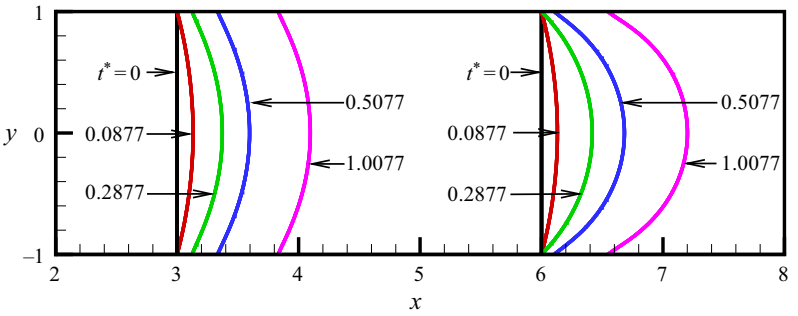


FIGURE 6. Snapshots of advancing and receding interfaces; $\Pi = 0.1$, $Ca = 0.01$. The dimensionless time step is set to $\Delta t^* = 10^{-4}$ initially and then gradually increases to 10^{-3}. Theoretically, the receding and advancing contact lines are depinned at $t^* = 0.0881$ and 0.2854, respectively, if the interfaces remain circular.

is very close to a circular arc, and θ_{app} defined above faithfully represents the interface behaviour at the macroscopic length scale.

5.2.1. *Transient behaviour of the contact line*

We consider a small capillary number $Ca = 0.01$, under which the interfaces remain almost circular. For convenience, we define a dimensionless time $t^* = t(\bar{V}/H)$ and length $x^* = x/H$.

A typical interface evolution is given in figure 6. At $t^* = 0$, the vertical interfaces correspond to $\theta_D = 90^\circ \in [\theta_R, \theta_A]$, and both contact lines are pinned. Under slow flow, each interface remains circular and $\theta_D = \theta_{app}$ when the contact line is pinned. We can thus easily find out the time instant to achieve a given θ_D by mass conservation and geometric relations, i.e.

$$t = \frac{1}{2}\frac{H}{\bar{V}}\left(\frac{\delta}{\sin^2\delta} - \cot\delta\right), \tag{5.4}$$

where $\delta = |\frac{\pi}{2} - \theta_D|$ is half of the central angle of the circular interface. Thus, theoretically, θ_D at the receding contact line achieves θ_R at $t^* = 0.0881$ and θ_D at the advancing contact line achieves θ_A at $t^* = 0.2854$. These values agree very well with the numerical ones, which are approximately $t^* = 0.0877$ and $t^* = 0.2877$. After these time instants the contact lines start to move, which is also manifested by figure 7.

The value of Π affects the effective slip and thus the contact line dynamics once the contact line moves. The transient behaviours for $\Pi = 0.01$, 0.1 and 1 are given in figures 7 and 8. It should be noted that, for each contact line, the curves for different Π values collapse in the beginning. After the contact line is depinned, the effect of Π kicks in and the curves start to deviate from each other.

In figure 7 each contact line starts to accelerate after it is depinned and eventually achieves the steady-state contact line velocity, which equals $\bar{V}$ due to mass conservation. After normalization, this velocity corresponds to a slope of 1 in figure 7. The only exception is the advancing contact line with $\Pi = 1$, where a steady state is never achieved and wetting failure occurs. Before reaching the steady state, the contact line velocity decreases as Π increases. This is easy to understand since the effective slip length decreases as Π increases (Yue & Feng 2011). In the context of the phase-field method, this trend can also be explained from energy dissipation: the dissipation rate associated

https://doi.org/10.1017/jfm.2020.465 Published online by Cambridge University Press

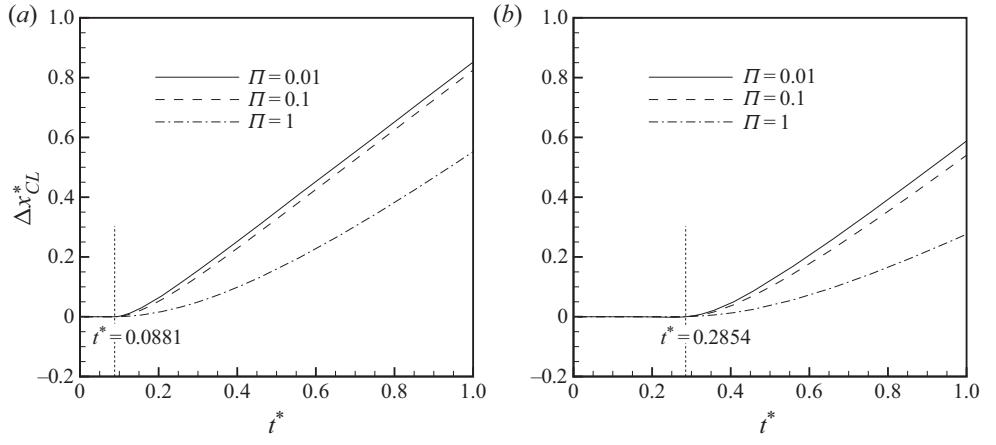


FIGURE 7. Displacements of contact lines; $Ca = 0.01$. Here Δx^*_{CL} is the normalized x-coordinate of the contact line relative to its initial position: (a) receding contact line and (b) advancing contact line.

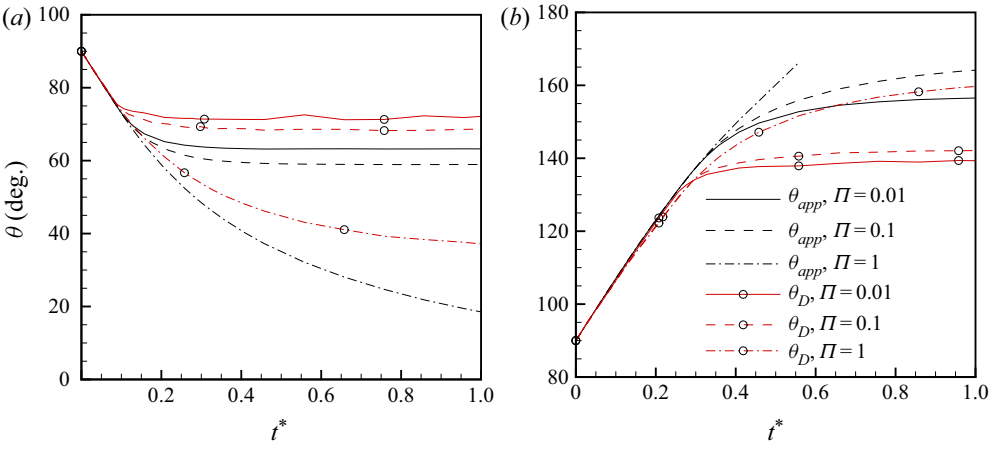


FIGURE 8. Transients of apparent and dynamic contact angles; $Ca = 0.01$: (a) receding contact line and (b) advancing contact line.

with the wall energy relaxation, $\int_{\partial\Omega_w} \Gamma\tilde{L}^2\,\mathrm{d}s = \int_{\partial\Omega_w} (1/\Gamma)(\mathrm{D}\phi/\mathrm{D}t)^2\,\mathrm{d}s$, is proportional to $\Pi \propto 1/\Gamma$ for the same amount of $\mathrm{D}\phi/\mathrm{D}t$; this additional dissipation slows down the contact line motion.

The transient behaviours of contact angles are given in figure 8. The dynamic contact angle θ_D is measured based on the $\phi = 0$ level curve in the first two layers of cells adjacent to the wall. Compared to θ_{app} from circular fitting, θ_D is more prone to numerical errors, as manifested by the oscillations in the θ_D curves with $\Pi = 0.01$ in both figures 8(a) and 8(b). As Π increases, both θ_D and θ_{app} deviate more from the static contact angle, consistent with the analysis in Yue & Feng (2011). For the advancing contact line with $\Pi = 1$, we terminate the θ_{app} curve around $t^* = 0.6$ because the radius of the circular fit to the interface drops below H. In this case, θ_{app} exceeds 180° and is no longer physical, which usually signifies the onset of wetting failure.

https://doi.org/10.1017/jfm.2020.465 Published online by Cambridge University Press

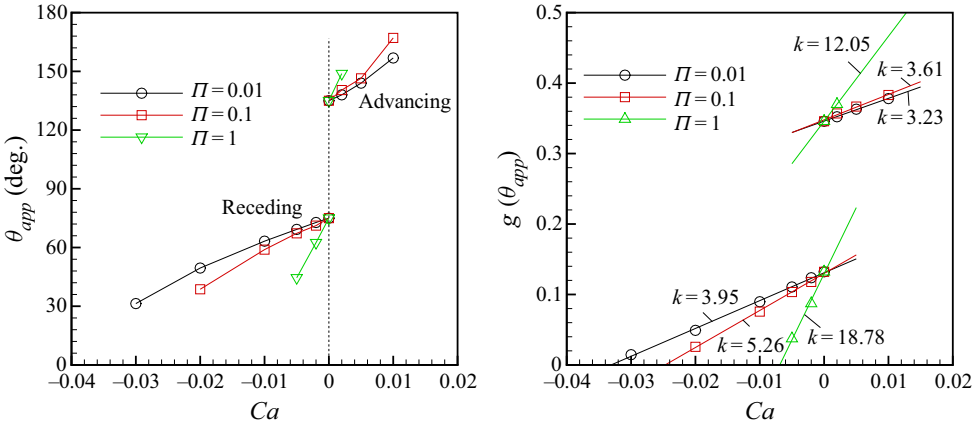


FIGURE 9. Steady-state dynamics of moving contact lines: $\theta_R = 75°$, $\theta_A = 135°$, $\lambda_\mu = 1$, $S = 0.01$, $Cn = 0.01$. The contact line advances if $Ca > 0$ and recedes if $Ca < 0$. The k values are the slopes of linear fits.

5.2.2. *Steady-state contact line dynamics*

From matched asymptotic analysis, Cox (1986) showed that, to the leading order, the apparent contact angle θ_{app} follows

$$g(\theta_{app}) = g(\theta_S) + Ca \ln\left(\frac{W}{l_s}\right), \tag{5.5}$$

where W is a characteristic macroscopic length, l_s is a slip length and Ca is the capillary number defined based on the advancing fluid. The function g is given by

$$g(\theta) = \int_0^\theta \frac{\mathrm{d}s}{f(s)},$$

where

$$f(\theta) = \frac{2\sin\theta\{\lambda_\mu^2(\theta^2 - \sin^2\theta) + 2\lambda_\mu[\theta(\pi - \theta) + \sin^2\theta] + [(\pi - \theta)^2 - \sin^2\theta]\}}{\lambda_\mu(\theta^2 - \sin^2\theta)[(\pi - \theta) + \sin\theta\cos\theta] + [(\pi - \theta)^2 - \sin^2\theta](\theta - \sin\theta\cos\theta)}$$

and λ_μ is the viscosity ratio between the receding and advancing fluids. The steady state apparent contact angle θ_{app} and the corresponding $g(\theta_{app})$ from phase-field simulations are given in figure 9, where the linear relation between $g(\theta_{app})$ and Ca is faithfully captured for both the advancing and receding contact lines at different Π values.

According to Yue *et al.* (2010), the slip length of the phase-field model due to interfacial mobility is approximately $2.5l_D$ for fluids with equal density. Furthermore, good agreements between Cox's formula and the phase-field method are achieved when W is taken to be the radius of the pipe for Poiseuille flows. For the plane Poiseuille flow considered here, it is then reasonable to take W to be the half-channel height H. When wall energy relaxation exists, the actual slip l_s differs from the $2.5l_D$. According to Yue & Feng (2011), we have

$$\frac{2\sqrt{2}}{3}\frac{\Pi}{Cn} = 5.63 \ln\left(\frac{2.5l_D}{\tilde{l}_s}\right) \tag{5.6}$$

https://doi.org/10.1017/jfm.2020.465 Published online by Cambridge University Press

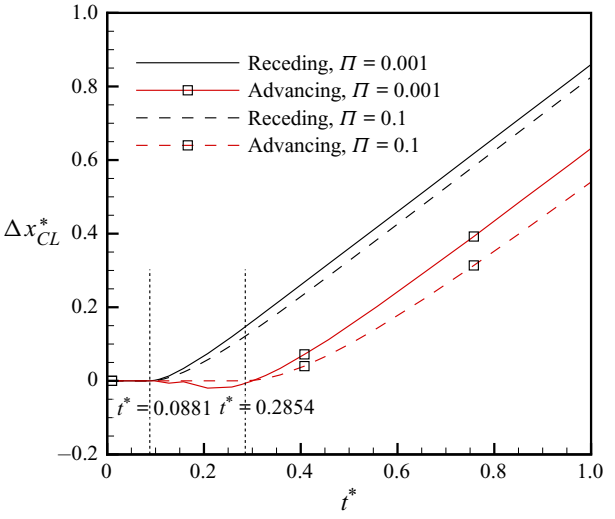


FIGURE 10. Pinning failure at a small Π; $\theta_R = 75^\circ$, $\theta_A = 135^\circ$, $Ca = 0.01$, $S = 0.01$, $Cn = 0.01$.

for θ_D close to 90°. Thus, the slope of the $g(\theta_{app}) \sim Ca$ curve should be

$$k = \ln\left(\frac{W}{l_s}\right) = \ln\left(\frac{H}{2.5l_D}\right) + \ln\left(\frac{2.5l_D}{\tilde{l}_s}\right) = \ln\left(\frac{1}{2.5S}\right) + \frac{2\sqrt{2}}{3}\frac{\Pi}{5.63Cn}.$$

This gives the theoretical slopes of $k = 3.86$, 5.36 and 20.44 for $\Pi = 0.01$, 0.1 and 1, respectively. These values agree reasonably well with the numerical values for the receding contact lines in figure 9(*b*). Much greater discrepancies are however observed on the advancing branch. This is probably because θ_D is too close to 180°. In this case, (5.6) is less accurate and we also expect larger errors in computing θ_{app}.

In summary, our current method captures the correct contact line dynamics, similar to the standard phase-field method without CAH (Yue *et al.* 2010; Yue & Feng 2011). The only complication is that θ_S may take different values, i.e. θ_R or θ_A, depending on whether the contact line recedes or advances.

5.2.3. *Pinning of the contact line and choice of Γ*

As we have mentioned before, the discretized weak form can not guarantee the exact satisfaction of (3.3). That is, in real calculations, the contact line may still move even when it is supposed to be pinned. This actually happens when Π (or $1/\Gamma$) is not sufficiently large, as shown in figures 10 and 11(*b*). The advancing contact line with $\Pi = 0.001$ recedes slightly when it is supposed to be pinned at $t^* < 0.2854$. At $t^* = 0.2577$, the contact line with $\Pi = 0.1$ is nicely pinned at $x^* = 6$ while that with $\Pi = 0.001$ shifts upstream by about two grid cells. A close inspection of figure 11(*b*) shows that the diffuse interface is slightly dilated near the wall. This type of pinning failure does not happen to the receding contact line, where the dynamic contact angle is very close to 90° before the contact line moves. Numerical tests with various contact angles and Π reveal that the pinning failure is more likely to occur for a smaller Π and when θ_D is further away from 90°.

https://doi.org/10.1017/jfm.2020.465 Published online by Cambridge University Press

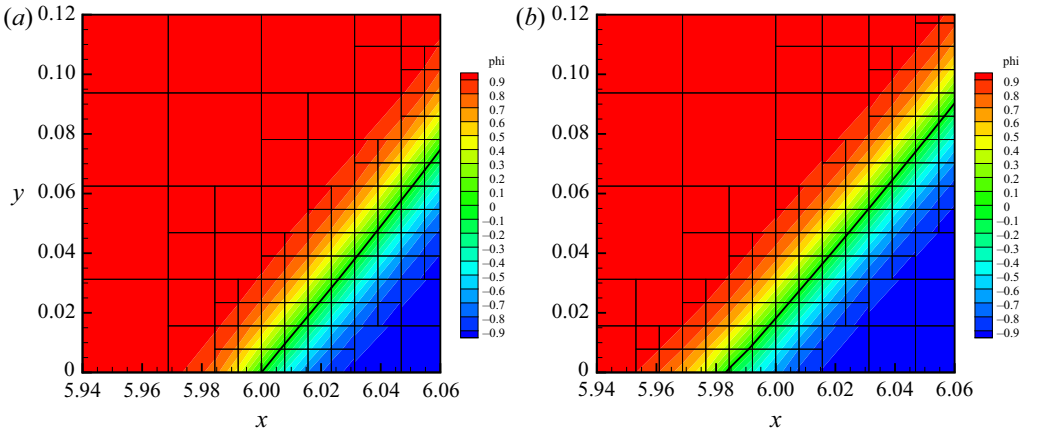


FIGURE 11. Plots of the ϕ contours at the vicinity of the advancing contact line at $t^* = 0.2577$; $\theta_R = 75^\circ$, $\theta_A = 135^\circ$, $Ca = 0.01$, $S = 0.01$, $Cn = 0.01$. (a) $\Pi = 0.1$, (b) $\Pi = 0.001$. The thick lines denote the interface ($\phi = 0$) and the thin lines are grid lines. The contact line is supposed to be pinned at $x^* = 6$.

To capture contact line pinning with good accuracy, we need a guideline for the choice of Π, i.e. Γ. By inspecting (4.12), we note that the energy dissipation rate on the solid wall $\partial\Omega_w$ for a pinned contact line can be written as

$$\mathcal{D}_w = \left(\frac{1}{\Gamma}\frac{\phi^{n+1}-\phi^n}{\Delta t}, \frac{\phi^{n+1}-\phi^n}{\Delta t}\right)_{\partial\Omega_w} - \left(\lambda \boldsymbol{n}\cdot\nabla\phi^{n+1/2} + Df_w(\phi^n, \phi^{n+1}; \theta_A), \frac{\phi^{n+1}-\phi^n}{\Delta t}\right)_{\partial\Omega_w} \tag{5.7}$$

and is supposed to be zero since $\phi^{n+1} = \phi^n$. However, in practice, $\phi^{n+1} = \phi^n$ is not guaranteed by the weak form and we have no control over the sign of the second term of $\mathcal{D}_w$. A negative dissipation $\mathcal{D}_w < 0$ may thus occur and lead to numerical instability. A positive dissipation can be achieved if the first term overpowers the second term, which can be roughly satisfied by $|(1/\Gamma)(\partial\phi/\partial t)| \gtrsim |\lambda \boldsymbol{n}\cdot\nabla\phi|$. For a contact line moving with speed V and angle θ_D, we have $|\partial\phi/\partial t| \sim V|\nabla\phi||\sin\theta_D|$ and $|\lambda \boldsymbol{n}\cdot\nabla\phi| \sim \sigma\epsilon|\nabla\phi||\cos\theta_D|$. This leads to the approximate criterion

$$\Pi \gtrsim \frac{Cn}{Ca}\cot\theta_D \tag{5.8}$$

for numerical stability.

We have tested different combinations of Π, Ca, Cn and S, with $\theta_R = 75^\circ$ and $\theta_A = 135^\circ$ being fixed. For the advancing contact line to falsely recede for the same displacement, Π has to be chosen such that it is proportional to Cn, inversely proportional to Ca and independent of S, i.e. $\Pi \propto Cn/Ca$.

To investigate the influence of θ_D, we take $\theta_A = 170^\circ$ so that pinning failure eventually occurs when θ_D is sufficiently close to 180°. We compute the advancing contact line with $\Pi = 0.001$, 0.01, 0.1, 0.2 and 0.5, until the contact line starts to move upstream for about one grid spacing h_{min}. Other parameters are kept constant: $Ca = 0.01$, $S = 0.01$ and $Cn = 0.01$. The instantaneous θ_D is then recorded as the critical value that causes pinning

https://doi.org/10.1017/jfm.2020.465 Published online by Cambridge University Press

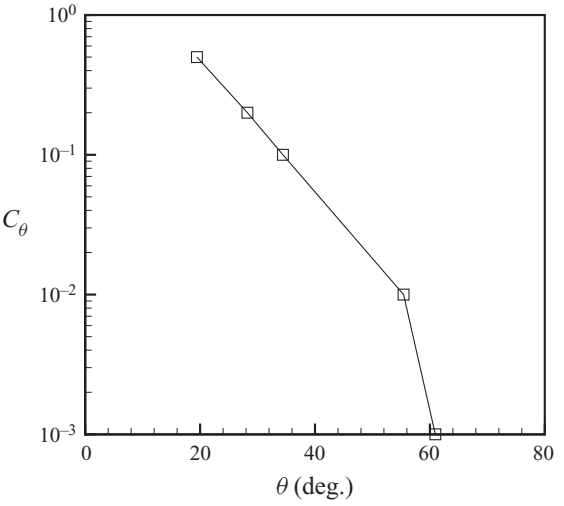


FIGURE 12. Numerical values of C_θ. $\theta = \min(\theta_D, \pi - \theta_D)$.

failure. We have also tested $\Pi = 1$, but pinning failure never occurs. The numerical results, however, do not suggest a linear relation between the Π and $\cot\theta_D$. If we relax (5.8) to

$$\Pi \gtrsim \frac{Cn}{Ca} C_\theta \tag{5.9}$$

then parameter C_θ can be numerically determined as shown in figure 12.

To achieve desired pinning performance in practical computations, we suggest using (5.9) together with figure 12 as a guideline for choosing Π. It should be noted that the derivations and numerical tests here are by no means rigorous.

5.2.4. *A computational strategy for hysteresis*

In the absence of CAH, a computational strategy has been proposed in Yue & Feng (2011) as follows. First, we choose a capillary width ϵ (or the dimensionless group Cn) based on the computational mesh that we can afford. Usually, we take $\epsilon \in [h_{min}, 2h_{min}]$, where h_{min} is the mesh size at the interface. This guarantees that the diffuse interface is sufficiently resolved. To reduce the influence of interfacial thickness on numerical results, Cn should be as small as possible, e.g. $Cn \leq 0.01$, which makes adaptive mesh refinement almost necessary. Second, we choose the mobility parameter M such that the diffusion length is well resolved: $l_D = \sqrt{M\mu} > \epsilon/4$ (or $S \geq Cn/4$ in the dimensionless form). This guarantees that the numerical results are independent of ϵ and h_{min}. Finally, we tune Γ (or the dimensionless group Π) to achieve the desired effective slip length.

This last step may however lead to a Π that is too small to numerically pin the contact line. Actually, the wall energy relaxation parameter Γ has no physical meaning when the contact line is pinned and we just need a non-zero number. Furthermore, there is no physical requirement that Γ must be a single-valued constant. We thus allow Γ to take different values depending on the status of the contact line and amend the third step above as follows. We estimate a Γ for pinning, denoted by Γ_P, based on (5.9) or numerical experiments. If Γ required for slip is greater than Γ_P then we impose Γ_P where the contact line is pinned and Γ elsewhere.

https://doi.org/10.1017/jfm.2020.465 Published online by Cambridge University Press

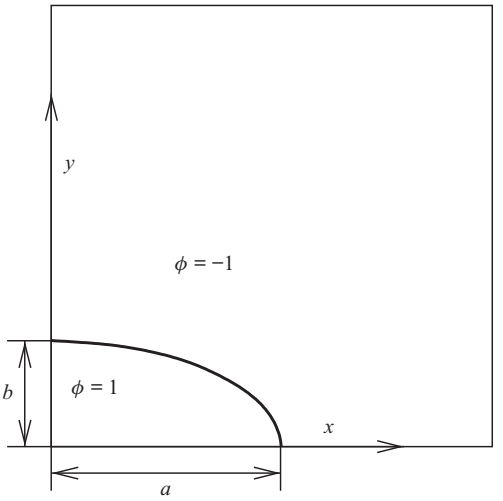


FIGURE 13. Schematic of an oscillating drop. The drop is initially elliptic with semi-axes $a = 2R_0$ and $b = 0.5R_0$, where R_0 is the effective drop radius.

5.3. *Oscillating drop*

In this subsection we consider an oscillating drop on a solid wall, where the contact line transitions between receding, pinning and advancing. A schematic of the computational set-up is given in figure 13. The initially elliptic drop will undergo oscillations due to inertia-capillary effects. The computational domain is a square of $4R_0 \times 4R_0$. Symmetry conditions are applied at the two vertical boundaries. Zero traction is applied on the upper boundary. The lower boundary is a solid wall with no-slip velocity and prescribed contact line conditions.

For convenience, we use effective drop radius R_0, drop density ρ_1 and surface tension σ to non-dimensionalize all the parameters, and denote the dimensionless parameters with a superscript *. For example, $t^* = t/t_c$, where $t_c = \sqrt{\rho R_0^3/\sigma}$ is the capillary time, viscosity $\mu^* = \mu/\sqrt{\rho_1 \sigma R_0}$ and energy $E^* = E/\sigma R_0$.

The fluid parameters are $\rho_1^* = 1$, $\rho_2^* = 0.01$, $\mu_1^* = 0.01$, $\mu_2^* = 0.001$ and $\sigma^* = 1$. This choice corresponds to a small Ohnesorge number

$$Oh = \frac{\mu_1}{\sqrt{\rho_1 \sigma R_0}} = 0.01, \tag{5.10}$$

such that the oscillation is not overdamped. For the diffuse interface, we choose $\epsilon^* = 0.01$, $M^* = 10^{-3}$ and $\Gamma^* = 10^3$. Some relevant dimensionless groups are $S = \sqrt{M\mu_1}/R_0 = 3.16 \times 10^{-3}$ and $\Pi = 1/\mu_1 \Gamma R_0 = 0.1$. For the computational mesh, we choose $h_{min}^* = \frac{1}{128}$ at the interface and $h_{max}^* = \frac{1}{4}$ in the bulk.

We run three simulations with different contact angles: $(\theta_R, \theta_A) = (90^\circ, 90^\circ)$, $(90^\circ, 105^\circ)$, $(75^\circ, 105^\circ)$. The evolution of the drop interface for $(90^\circ, 105^\circ)$ and $(90^\circ, 90^\circ)$ are shown in figures 14 and 15, respectively. In the initial stage, the contact line moves to the left (i.e. recedes), and its dynamics is controlled by θ_R solely. Therefore, these two cases are identical before the contact line stops at the leftmost position at $t^* \approx 1.723$. This is also manifested by the overlapping curves at $t^* \lesssim 1.723$ in figures 16 and 17. For $(\theta_R, \theta_A) = (90^\circ, 105^\circ)$, the contact line is pinned for a short period (around $t \in [1.723, 1.960]$) while the interface continues to protrude to the right. Once θ_D reaches

https://doi.org/10.1017/jfm.2020.465 Published online by Cambridge University Press

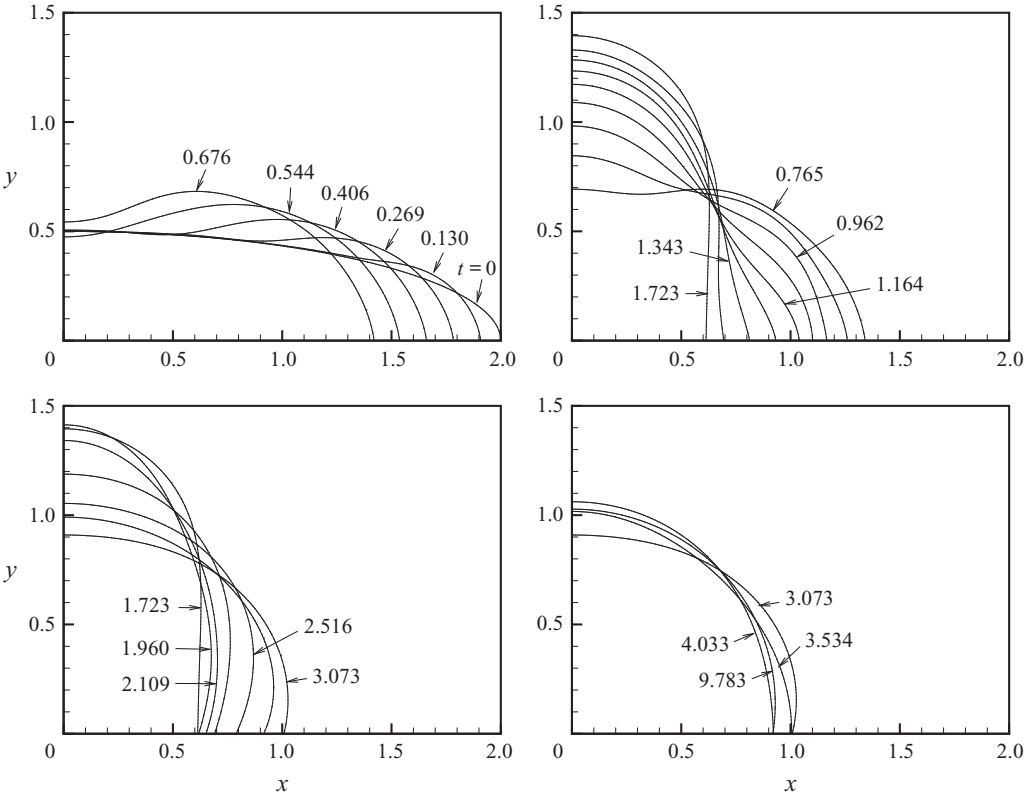


FIGURE 14. Snapshots of an oscillating drop with CAH; $\theta_R = 90^\circ$, $\theta_A = 105^\circ$. The contact line is pinned at $t^* \in [1.723, 1.960]$, $[3.073, 3.534]$ and $[4.033, \infty)$.

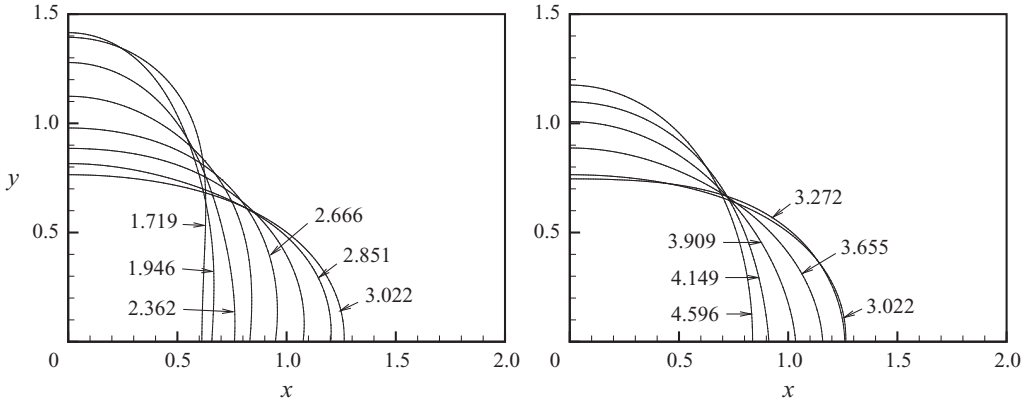


FIGURE 15. Snapshots of an oscillating drop without CAH; $\theta_R = \theta_A = 90^\circ$.

105° ($t \approx 1.960$), the contact line starts to move rightward. The contact line is pinned again around $t \in [3.073, 3.0534]$, and then retracts. Finally, the contact line stays pinned after $t^* = 4.033$ while the other part of the interface keeps oscillating. In contrast, there is no obvious contact line pinning for $(\theta_R, \theta_A) = (90^\circ, 90^\circ)$, i.e. when there is no CAH.

https://doi.org/10.1017/jfm.2020.465 Published online by Cambridge University Press

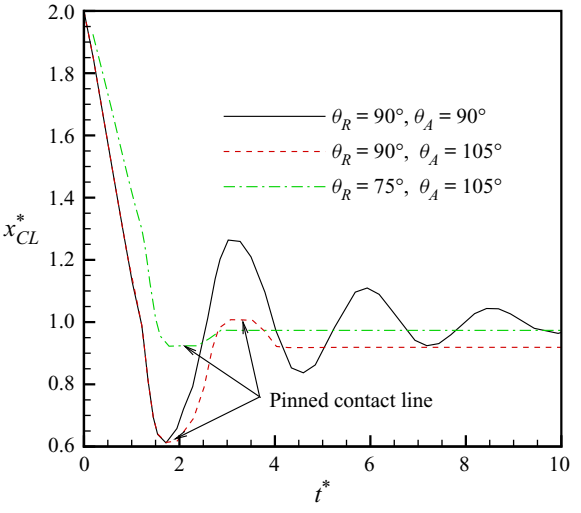


FIGURE 16. Contact line positions of oscillating drops. The plateaus denote the pinning of contact lines.

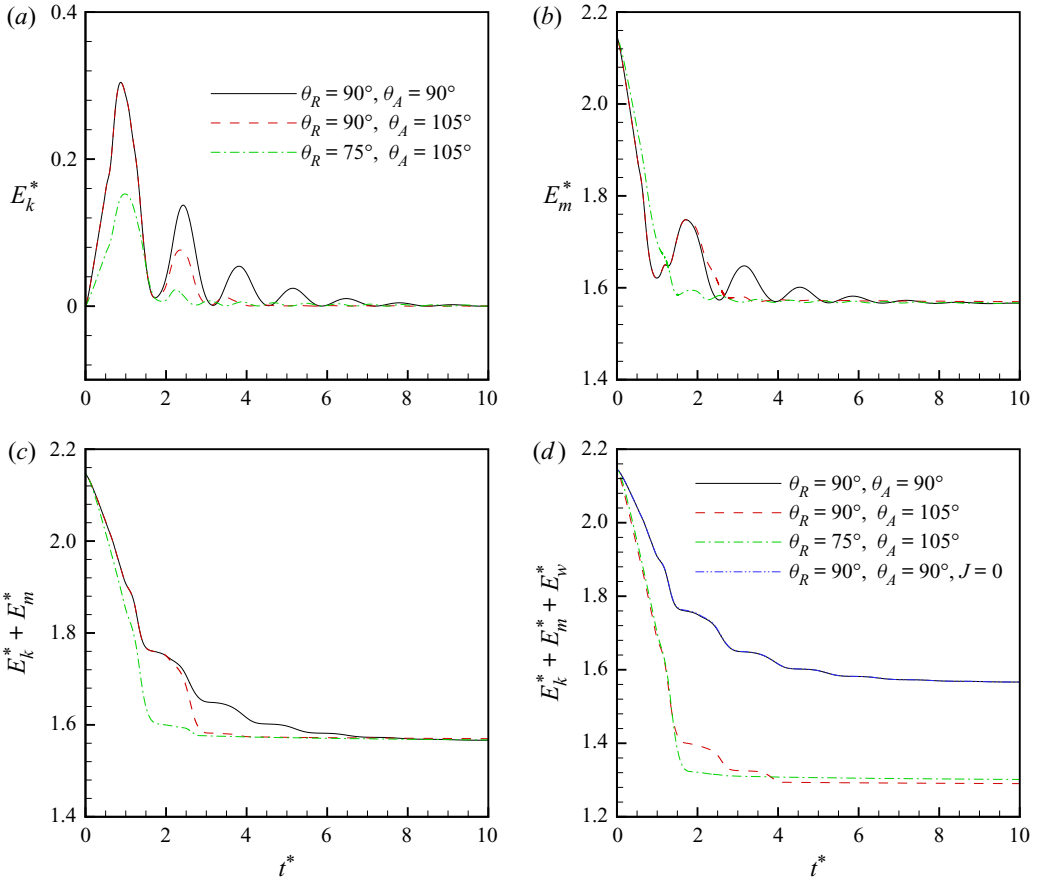


FIGURE 17. Time history of dimensionless free energies of oscillating drops: (*a*) kinetic energy, (*b*) mixing energy, (*c*) total energy excluding wall energy and (*d*) total energy.

https://doi.org/10.1017/jfm.2020.465 Published online by Cambridge University Press

At $t^* \to \infty$, the drop will eventually settle to a static circular shape. The contact line position, i.e. the spreading radius, is related to the θ_{app} (which is also the same as θ_D) by

$$x^*_{CL} = \sqrt{\frac{\pi}{2[\theta_{app} - \frac{1}{2}\sin(2\theta_{app})]}}\sin\theta_{app}.$$

This gives $x^*_{CL} = 1.176$, 1 and 0.839 for $\theta_{app} = 75^\circ$, 90° and 105°, respectively. The trajectories of the contact line are given in figure 16. It is obvious that the contact line keeps oscillating around $x^*_{CL} = 1$ when there is no CAH. When there exists CAH, the contact line is finally pinned at $x^*_{CL} = 0.919$ and 0.973 for $(\theta_R, \theta_A) = (90^\circ, 105^\circ)$ and $(75^\circ, 105^\circ)$, both in the range determined by θ_R and θ_A. But the exact location of the final x^*_{CL} is also dependent on the transient process, i.e. the history of the contact line.

The evolution of free energies are given in figure 17. Here, the dimensionless free energies are computed as follows: kinetic energy $E^*_k = \int_\Omega \frac{1}{2}\rho|\boldsymbol{u}|^2\,\mathrm{d}\boldsymbol{x}/(\sigma R_0)$, mixing energy $E^*_m = \int_\Omega f_m\,\mathrm{d}\boldsymbol{x}/(\sigma R_0)$ and wall energy $E^*_w = \int_{\partial\Omega_w} f_w(\phi;\theta_A)\,\mathrm{d}s/(\sigma R_0)$. At $t^* = 0$, the whole system is static, which corresponds to a zero kinetic energy E^*_k and a maximum mixing energy E^*_m. As the drop retracts, part of the mixing energy is converted into kinetic energy. The repeated conversions between mixing and kinetic energies are manifested by the oscillatory curves in figures 17(*a*) and 17(*b*). As time approaches $t^* = 10$, E^*_k drops to zero while E^*_m stabilizes around 1.57. The latter is consistent with the surface energy of a drop with $\theta_{app} = 90^\circ$: $(\pi/2)\sigma R_0^2 = 1.571\sigma R_0^2$. The two curves with CAH stabilize much faster than the one without due to additional dissipation from CAH.

In the initial retraction stage ($t^* \lesssim 1.723$), the E^*_k curve for $\theta_R = 75^\circ$ deviates from the other two because contact line dynamics is determined by θ_R. Similarly, the sum $E^*_k + E^*_m$ decreases faster for $\theta_R = 75^\circ$ in the initial retraction stage, as shown in figure 17(*c*). The evolution of the total free energy is provided in figure 17(*d*) to demonstrate the energy dissipative nature of our model. Although we can only prove the discrete energy law (4.12) for matched density and zero CAH, the numerical solutions satisfy a dissipative discrete energy law for a broader choice of parameters.

We also investigate the influence of the diffusive flux $\boldsymbol{J}$ on the phase-field simulations of interfacial flows with non-matched densities. We set $\boldsymbol{J} = 0$, i.e. neglecting the diffusive flux as in many previous phase-field simulations (e.g. Jacqmin 1999; Villanueva & Amberg 2006; Yue *et al.* 2006; Khatavkar *et al.* 2007*a*), and show the result for $\theta_R = \theta_A = 90^\circ$ in figure 17(*d*). The curve with $\boldsymbol{J} = 0$ is almost identical to the one considering diffusive flux. This is not surprising because the diffusive flux only occurs in the diffuse-interface region and its effect diminishes as Cn decreases. Thus, in interfacial flows with non-matched densities we expect the diffusive flux $\boldsymbol{J}$ to be negligible, at least in the case of $Cn \ll 1$.

5.4. *Three-dimensional drop on an inclined wall*

Our code can be easily switched to three dimensions, thanks to the dimension-independent programming advocated in deal.ii (Bangerth 2000). However, the discrete system resulting from the mixed finite element method is very costly to solve and thus we can only perform some preliminary 3-D simulations. A more efficient projection-based flow solver is currently under development. The purpose of this subsection is only to demonstrate the capability of our hysteresis model in 3-D flows.

We consider a drop on an inclined wall, as shown in figures 18 and 19. Similar to § 5.3, we use drop density ρ_1, surface tension σ and drop radius R_0 to non-dimensionalize

https://doi.org/10.1017/jfm.2020.465 Published online by Cambridge University Press

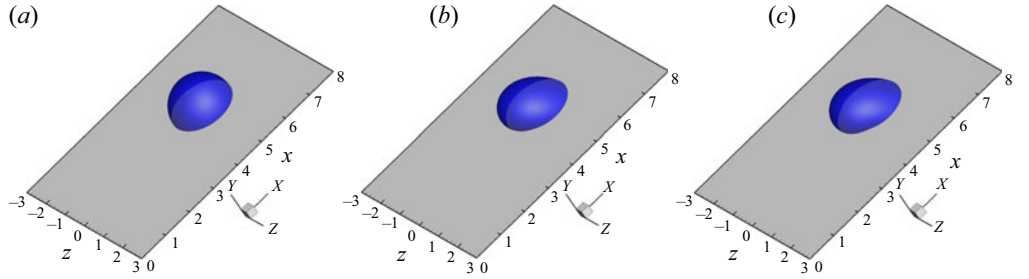


FIGURE 18. Three-dimensional drop sticking to an inclined wall; $Bo = 0.99$: (*a*) $t^* = 0$, (*b*) $t^* = 4.52$ and (*c*) $t^* = 24.52$.

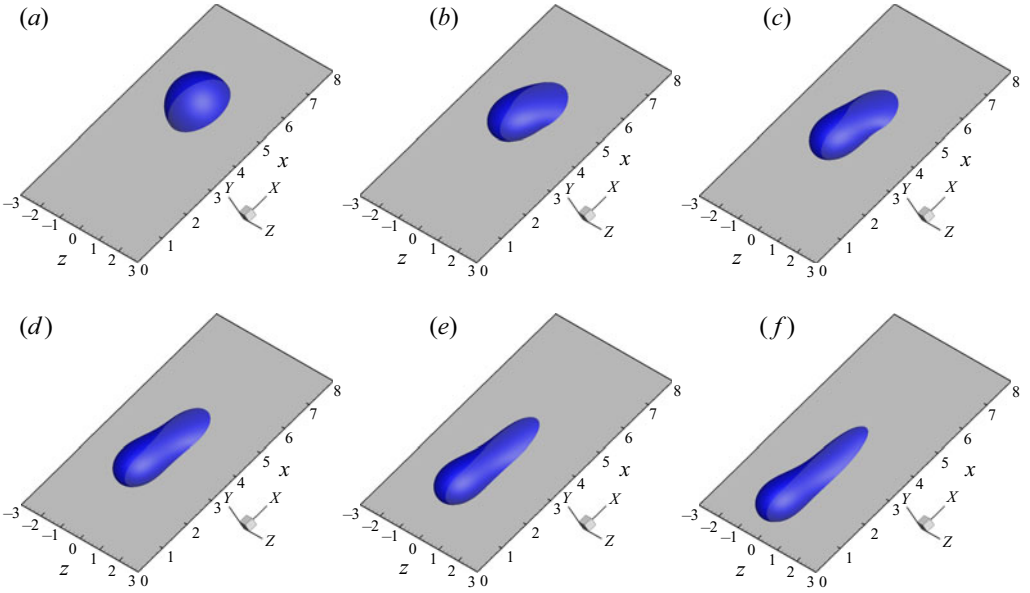


FIGURE 19. Three-dimensional drop sliding on an inclined wall; $Bo = 1.98$: (*a*) $t^* = 0$, (*b*) $t^* = 4.52$, (*c*) $t^* = 14.52$, (*d*) $t^* = 24.52$, (*e*) $t^* = 34.52$ and (*f*) $t^* = 44.52$.

all parameters. Owing to symmetry in the z-direction, we only compute half of the drop. The computational domain is a rectangular box defined by $[0, 8] \times [0, 3] \times [0, 3]$ with a hemispherical drop initially centred at $(5, 0, 0)$. The following dimensionless parameters are adopted: $\rho_1^* = 1$, $\rho_2^* = 0.01$, $\mu_1^* = 1$, $\mu_2^* = 0.01$, $\sigma^* = 1$, $R_0^* = 1$, $\epsilon^* = 0.02$, $M^* = 10^{-4}$, $\theta_R = 60^\circ$, $\theta_A = 120^\circ$, $\Gamma^* = 100$ and slope inclination angle $\alpha = 60^\circ$. These parameters correspond to the following dimensionless groups: $Cn = \epsilon/R_0 = \epsilon^* = 0.02$, $S = \sqrt{M\mu_1}/R_0 = \sqrt{M^*} = 10^{-2}$, $\Pi = 1/\mu_1 \Gamma R_0 = 1/\Gamma^* = 0.01$ and $Oh = \mu_1/\sqrt{\rho_1 \sigma R_0} = 1$. We test $g^* = 1$ and $g^* = 2$, which correspond to the Bond numbers $Bo = (\rho_1 - \rho_2) g R_0^2/\sigma = (1 - \rho_2^*) g^* = 0.99$ and 1.98, respectively. For the computational mesh, we choose $h_{min}^* = \frac{1}{64}$ at the interface and $h_{max}^* = \frac{1}{8}$ in the bulk. The time step is set to $\Delta t^* = 0.01$ initially and is gradually increased to $\Delta t^* = 0.05$.

To achieve a good pinning performance, we take a smaller wall energy relaxation parameter $\Gamma_P^* = 10$ (such that $\Pi_P = 0.1$) when the contact line is pinned. It should be noted that this problem does not have a well-defined capillary number when the drop is

https://doi.org/10.1017/jfm.2020.465 Published online by Cambridge University Press

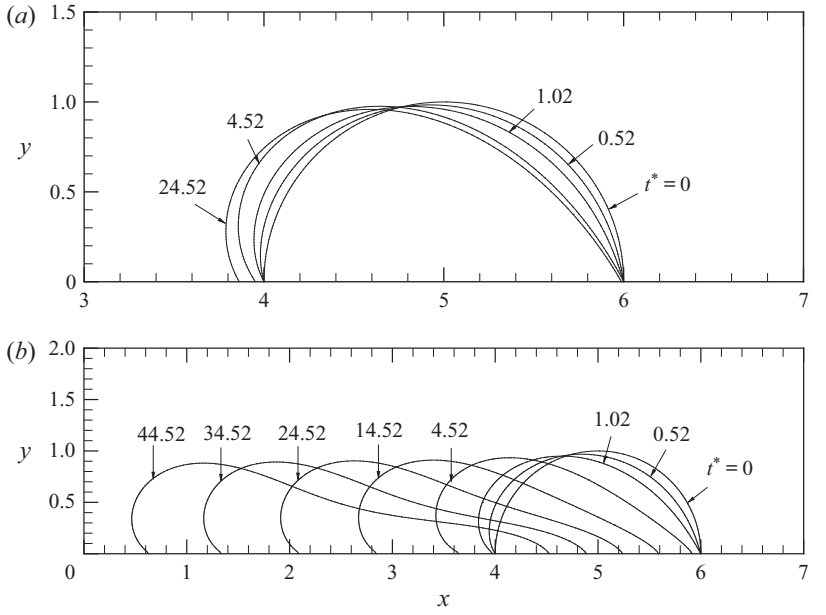


FIGURE 20. Side views of 3-D drops on an inclined wall: (*a*) $Bo = 0.99$ and (*b*) $Bo = 1.98$.

pinned as shown in figure 18. In this case, we can do a rough estimation. Suppose we want the pinned contact line to move less than the grid spacing h^*_{min} during the whole simulation that lasts for $t^* \sim 20$. This gives $Ca \sim 10^{-3}$ and then (5.9) predicts $\Pi \gtrsim 0.02$ if we take $C_\theta = 0.001$ based on figure 12. Thus, $\Pi_P = 0.1$ should be a safe choice.

It is well known that, due to CAH, relatively small drops have a tendency to stick to solid surfaces even when the latter is tilted. The critical parameters for the onset of drop sliding satisfy

$$(\rho_1 - \rho_2) V_d g \sin\alpha = w\sigma(\cos\theta_R - \cos\theta_A), \tag{5.11}$$

where V_d is the volume of the drop and w is the width of the drop. This relation was first given by Furmidge (1962) based on experimental observations, and was later proved to be exact by Dussan V. & Chow (1983) as long as the footprint of the drop is convex. In practice, w is dependent on drop deformation and is unknown *a priori*. However, for an initially hemispherical drop, we can take the approximation $w \approx 2R_0$. This leads to the critical Bond number

$$Bo_c = \frac{\cos\theta_R - \cos\theta_A}{\frac{\pi}{3}\sin\alpha}, \tag{5.12}$$

which is 1.1027 for our chosen angles. It should be noted that Bo_c in the real situation may be more complicated and a problem-dependent prefactor needs to be included (Janardan & Panchagnula 2014).

Theoretically, the drop with $Bo = 0.99$ should stick to the slope while the drop with $Bo = 1.98$ should slide. This is confirmed by our numerical results in figures 18 and 19. The side views of the drops are given in figure 20, where the initial pinning of the contact line is observed for both Bond numbers. It should be noted that the contact line in (*a*) moves slightly because of the initial transient and the fact that $Bo = 0.99$ is very close to the critical value. The top views of the drops, i.e. the contact lines, are given in figure 21. Theoretically, we expect a steadily sliding drop to have two straight sides parallel to the

https://doi.org/10.1017/jfm.2020.465 Published online by Cambridge University Press

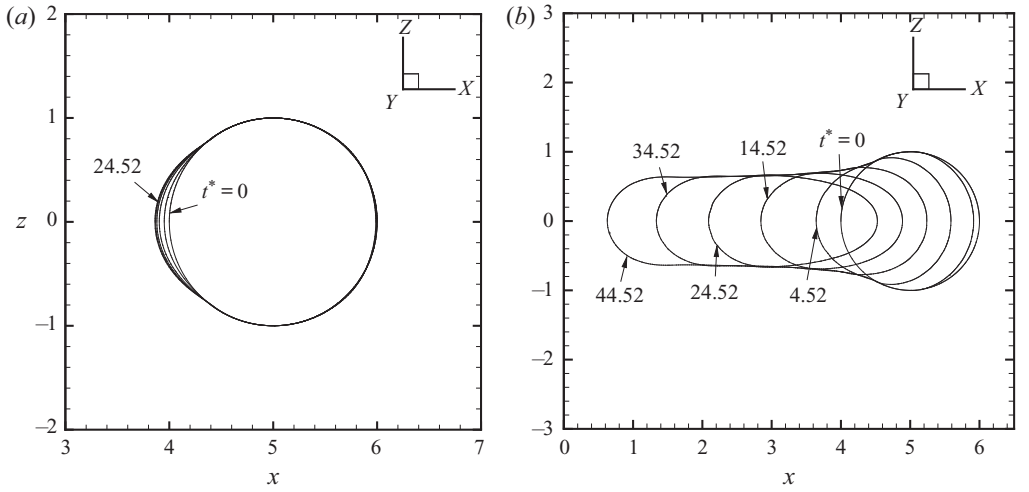


FIGURE 21. Evolution of contact lines: (*a*) $Bo = 0.99$ and (*b*) $Bo = 1.98$.

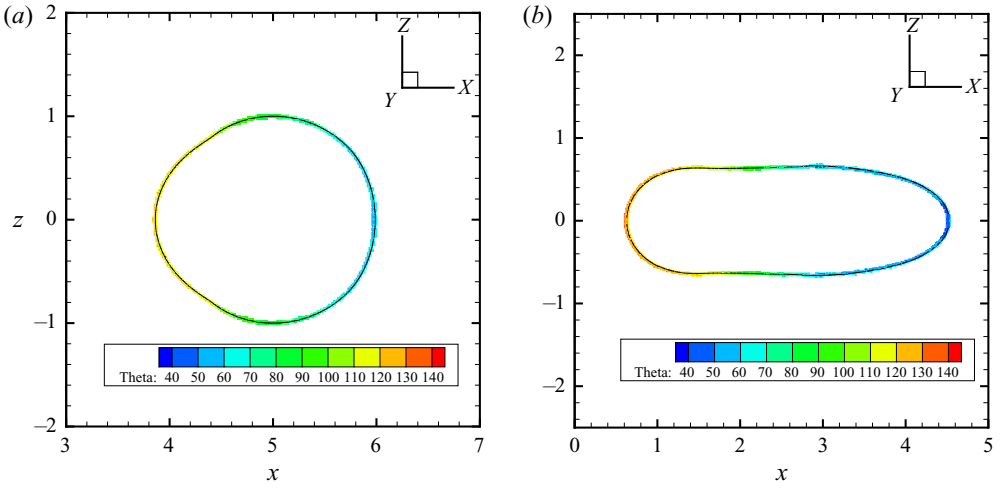


FIGURE 22. Dynamic contact angle: (*a*) $Bo = 0.99$, $t^* = 24.52$ and (*b*) $Bo = 1.98$, $t^* = 44.52$.

moving direction (Furmidge 1962; Eral *et al.* 2013). This trend can be found from the contact line shape at $t^* = 44.52$. It should be noted that we have to terminate the simulation before a steady state was achieved because of the small computational domain. We will leave computations with realistic fluid properties and a larger computational domain for future work when a much more efficient flow solver is ready.

In the end we investigate the dynamic contact angle θ_D. It is difficult to directly measure θ_D based on the level surface of $\phi = 0$ in three dimensions. We thus compute θ_D based on the relation $\cos\theta_D = (\boldsymbol{n} \cdot \nabla\phi)/|\nabla\phi|$ and the results are shown in figure 22. For the static drop in (*a*), $\theta_D \in [60^\circ, 120^\circ]$ along the whole contact line, consistent with the pinning condition. For the sliding drop in (*b*), $\theta_D > 120^\circ$ at the leading edge, $\theta_D < 160^\circ$ at the trailing edge and $\theta_D \in [60^\circ, 120^\circ]$ along majority of the two sides. Correspondingly, the

https://doi.org/10.1017/jfm.2020.465 Published online by Cambridge University Press

contact line advances at the leading edge, recedes at the trailing edge and is pinned at the two sides as expected.

6. Concluding remarks

We have developed an energy-based boundary condition for CAH. The wall energy relaxation allows the two-phase system to deviate from equilibrium at the contact line. As a result, the microscopic dynamic contact angle θ_D, which is computed by the phase-field method, may differ from the prescribed static angle θ_S. The tendency of contact line motion can then be deduced from the difference between these two angles. When CAH exists, the single valued θ_S is extended to a range of angles, namely, the hysteresis window $[\theta_R, \theta_A]$. Similarly, the tendency of contact line motion can be readily obtained from the computed θ_D and the prescribed θ_R and θ_A: the contact line advances if $\theta_D > \theta_A$, recedes if $\theta_D < \theta_R$ and is pinned otherwise. The major conclusions are summarized as follows.

(i) In the phase-field method the relations between θ_D, θ_R and θ_A can be directly obtained from the values of the wall potentials defined based on θ_R and θ_A. As a result, our method captures CAH automatically, without the need to compute the contact line velocity or the dynamic contact angle.

(ii) When the contact line moves, our method automatically picks θ_R or θ_A depending on whether the contact line recedes or advances. The resulting contact line dynamics is exactly the same as the one without hysteresis. Furthermore, it agrees quantitatively with the well-established Cox theory.

(iii) The whole equation system satisfies a dissipative energy law and is thermodynamically consistent. In particular, the dissipation due to CAH is faithfully accounted for. Our Galerkin-type numerical discretization inherits this energy-dissipative property and is unconditionally energy stable for matched density and zero hysteresis. Numerical tests show that the numerical scheme remains energy dissipative for a broader range of parameters.

(iv) The wall energy relaxation parameter Γ is the only free parameter that can be tuned. We have provided a guideline for Γ to achieve good pinning performance when the contact line is pinned and to produce desired effective slip when the contact line is in motion.

(v) Our method has no limitation on dimensionality and it can be directly applied to three-dimensional flows.

The proposed method is easy to implement. If one has a phase-field code that allows wall energy relaxation then hysteresis can be easily added with one additional copy of wall potential. Since wall potentials are only evaluated on the wall boundary, the additional computational cost is almost negligible.

A key component of our method is the dynamic contact angle θ_D that is computed and may deviate from θ_S. The same idea can be extended to Ren and E's version of GNBC (Ren & E 2007, 2011*a*), which also works for sharp-interface methods. We have developed a level-set method for CAH based on Ren and E's slip condition, and more details can be found in Zhang & Yue (2020).

Acknowledgments

This work was supported by the National Science Foundation (grant DMS-1522604). The author thanks J. J. Feng at the University of British Columbia for insightful comments on the draft of this manuscript. The author also acknowledges Advanced Research

https://doi.org/10.1017/jfm.2020.465 Published online by Cambridge University Press

Computing at Virginia Tech for providing computational resources and technical support that have contributed to the results in this work.

Declaration of interests

The author reports no conflict of interest.

Appendix A. Wall energy and contact angle

In this section we provide a brief derivation of the wall energy formulation that is consistent with the ϕ profile across the diffuse interface. We consider a planar interface that intersects the wall with angle θ_S and assume the whole system to be in static equilibrium, as shown in figure 23.

The equilibrium of the diffuse interface with mixing energy (2.2) requires

$$G = \lambda\left(-\frac{\mathrm{d}^2\phi}{\mathrm{d}\xi^2} + f_0'(\phi)\right) = 0, \tag{A 1}$$

where we have considered the fact that ϕ is only dependent on ξ for the planar interface (Yue *et al.* 2004). Multiplying this equation by $\mathrm{d}\phi/\mathrm{d}\xi$ gives

$$\frac{1}{2}\frac{\mathrm{d}}{\mathrm{d}\xi}\left(\frac{\mathrm{d}\phi}{\mathrm{d}\xi}\right)^2 = \frac{\mathrm{d}f_0}{\mathrm{d}\xi}. \tag{A 2}$$

Since $f_0 = 0$ and $\mathrm{d}\phi/\mathrm{d}\xi = 0$ at $\xi = \pm\infty$, this equation can be integrated to give

$$\frac{\mathrm{d}\phi}{\mathrm{d}\xi} = \sqrt{2f_0} = \frac{1-\phi^2}{\sqrt{2}\epsilon}. \tag{A 3}$$

It should be noted that the hyperbolic tangent profile $\phi(\xi) = \tanh(\xi/\sqrt{2}\epsilon)$ can be obtained by further integrating (A 3) and taking $\phi(\pm\infty) = \pm 1$.

When the planar interface intersects the wall with angle θ_S, we get

$$\lambda\boldsymbol{n}\cdot\nabla\phi = \lambda(\boldsymbol{n}\cdot\boldsymbol{e}_\xi)\frac{\mathrm{d}\phi}{\mathrm{d}\xi} = \lambda\cos\theta_S\frac{1-\phi^2}{\sqrt{2}\epsilon} = \frac{3}{4}\sigma\cos\theta_S(1-\phi^2), \tag{A 4}$$

where $\boldsymbol{e}_\xi = \nabla\phi/|\nabla\phi|$ is the unit vector in the direction of ξ and we have used $\sigma = (2\sqrt{2}/3)(\lambda/\epsilon)$. Meanwhile, the equilibrium at the contact line requires

$$L(\phi, \nabla\phi; \theta_S) = \lambda\boldsymbol{n}\cdot\nabla\phi + f_w'(\phi) = 0, \tag{A 5}$$

from which we can obtain the wall energy

$$f_w(\phi) = -\int\frac{3}{4}\sigma\cos\theta_S(1-\phi^2)\,\mathrm{d}\phi = -\sigma\frac{\phi(3-\phi^2)}{4}\cos\theta_S + c, \tag{A 6}$$

where c is an integration constant. Theoretically, c is determined by the interfacial tensions between the fluids and the solid wall. However, the exact value of c does not matter in practice, since we only care about the variation in free energy rather than its absolute value. We simply take $c = 0$ in our simulations.

When a planar interface intersects the wall with a dynamic angle θ_D, similar to (A 4),

https://doi.org/10.1017/jfm.2020.465 Published online by Cambridge University Press

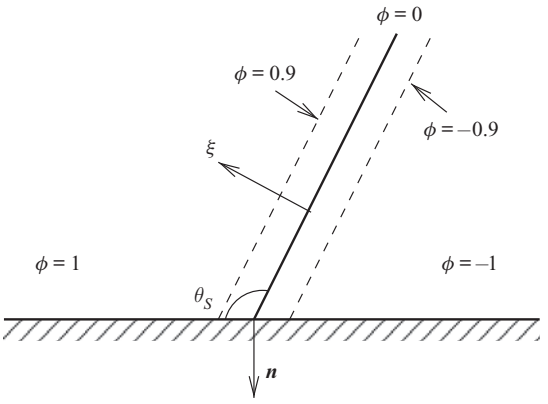


FIGURE 23. Schematic of a contact line formed by a planar interface at static equilibrium. Here ξ is the local coordinate in the direction of $\nabla\phi$ with $\xi = 0$ at the centre of the diffuse interface and $\boldsymbol{n}$ is the unit normal to the solid wall. The contours of ϕ are parallel lines intersecting the solid wall with θ_S.

we obtain

$$\lambda \boldsymbol{n} \cdot \nabla\phi = \lambda \cos\theta_D \frac{1-\phi^2}{\sqrt{2}\epsilon} = -f_w'(\phi; \theta_D), \tag{A 7}$$

which is used in § 3 to determine the relation between θ_D and the static contact angles θ_A and θ_R. Here the definition of $f_w(\phi; \theta)$ is given in (3.1). It should be noted that other forms of wall energy that do not satisfy (A 6), e.g. those in Qian, Wang & Sheng (2006*b*), Gao & Wang (2014) and Luo *et al.* (2017), may lead to distortions of ϕ contours at the contact line and cannot guarantee (A 7).

Appendix B. Constitutive relations in the phase-field model

In this section, motivated by the work of Ren & E (2011*b*) and the review article of Gomez & van der Zee (2017), we derive the constitutive relations in moving contact line problems based on thermodynamic principles. The same technique was also used in de Gennes & Prost (1993) to pose constitutive laws for nematic liquid crystals. Different from the work in Ren & E (2011*b*), we consider a general fluid domain without requiring $\boldsymbol{n} \cdot \boldsymbol{u} = 0$ on the boundary.

For an incompressible two-phase system in contact with a solid wall, the total free energy can be written as

$$\mathcal{F} = \int_\Omega \left(f_m(\phi, \nabla\phi) + \frac{1}{2}\rho|\boldsymbol{u}|^2 \right) \mathrm{d}\boldsymbol{x} + \int_{\partial\Omega_w} f_w(\phi)\, \mathrm{d}s, \tag{B 1}$$

where f_m is the mixing energy per unit volume, f_w is the surface energy per unit area on the wall, Ω is the domain occupied by the two-phase system and $\partial\Omega_w \subset \partial\Omega$ denotes the solid wall surface which can only perform rigid-body motion. Here we have neglected external forces such as gravity, which can be easily accounted for. The fluid domain Ω is advected by fluid velocity $\boldsymbol{u}$ and $\partial\Omega_w$ by wall velocity $\boldsymbol{u}_w$. For an impermeable wall, $\boldsymbol{n} \cdot (\boldsymbol{u} - \boldsymbol{u}_w) = 0$ is satisfied, where $\boldsymbol{n}$ is the outward pointing unit normal to the boundary. We define slip velocity $\boldsymbol{u}_s = \boldsymbol{u} - \boldsymbol{u}_w$, and then impermeability yields $\boldsymbol{u}_s \cdot \boldsymbol{n} = 0$.

https://doi.org/10.1017/jfm.2020.465 Published online by Cambridge University Press

Different conventions have been used for tensor operations. In this work we follow Soutas-Little (1999) and define the tensor operations as follows: $(\boldsymbol{A}\cdot\boldsymbol{B})_{ik}=A_{ij}B_{jk}$, $\boldsymbol{A}:\boldsymbol{B}=A_{ij}B_{ij}$, $(\boldsymbol{a}\cdot\boldsymbol{A})_j=a_iA_{ij}$, $(\boldsymbol{A}\cdot\boldsymbol{a})_i=A_{ij}a_j$, $(\boldsymbol{a}\otimes\boldsymbol{b})_{ij}=a_ib_j$, $(\nabla\boldsymbol{a})_{ij}=(\partial/\partial x_i)a_j$, and $(\nabla\cdot\boldsymbol{A})_j=(\partial/\partial x_i)A_{ij}$. Here $\boldsymbol{A}$ and $\boldsymbol{B}$ are second-order tensors, $\boldsymbol{a}$ and $\boldsymbol{b}$ are vectors, and we have used the Einstein summation convention over repeated indices.

The flow needs to satisfy mass conservation

$$\frac{\partial\rho}{\partial t}+\nabla\cdot(\rho\boldsymbol{u})=0, \tag{B 2}$$

and the momentum equation

$$\rho\frac{D\boldsymbol{u}}{\mathrm{D}t}=\nabla\cdot\boldsymbol{T}, \tag{B 3}$$

where $\boldsymbol{T}$ is the stress term to be determined later and $D/\mathrm{D}t=\partial/\partial t+\boldsymbol{u}\cdot\nabla$ denotes the material derivative. To conserve mass of each phase, we adopt the following equation for ϕ:

$$\frac{\mathrm{D}\phi}{\mathrm{D}t}=-\nabla\cdot\boldsymbol{j}. \tag{B 4}$$

Here $\boldsymbol{j}$ is a diffusive flux to be determined. For simplicity, we assume zero diffusive flux on the whole boundary $\partial\Omega$: $\boldsymbol{n}\cdot\boldsymbol{j}=0$.

For the mixing energy, following the Reynolds transport theorem, we obtain

$$\begin{aligned}\frac{\mathrm{d}}{\mathrm{d}t}\int_\Omega f_m\,\mathrm{d}\boldsymbol{x}&=\int_\Omega\left(\frac{\partial f_m}{\partial t}+\nabla\cdot(\boldsymbol{u}f_m)\right)\mathrm{d}\boldsymbol{x}\\&=\int_\Omega\left[\frac{\partial f_m}{\partial\phi}\frac{\partial\phi}{\partial t}+\frac{\partial f_m}{\partial\nabla\phi}\cdot\frac{\partial\nabla\phi}{\partial t}+\boldsymbol{u}\cdot\left(\frac{\partial f_m}{\partial\phi}\nabla\phi+\frac{\partial f_m}{\partial\nabla\phi}\cdot(\nabla\nabla\phi)\right)+f_m\nabla\cdot\boldsymbol{u}\right]\mathrm{d}\boldsymbol{x}\\&=\int_\Omega\left[\left(\frac{\partial f_m}{\partial\phi}-\nabla\cdot\frac{\partial f_m}{\partial\nabla\phi}\right)\left(\frac{\partial\phi}{\partial t}+\boldsymbol{u}\cdot\nabla\phi\right)+\left(f_m\boldsymbol{I}-\frac{\partial f_m}{\partial\nabla\phi}\otimes\nabla\phi\right):\nabla\boldsymbol{u}\right]\mathrm{d}\boldsymbol{x}\\&\quad+\oint_{\partial\Omega}\boldsymbol{n}\cdot\frac{\partial f_m}{\partial\nabla\phi}\left(\frac{\partial\phi}{\partial t}+\boldsymbol{u}\cdot\nabla\phi\right)\mathrm{d}s.\end{aligned} \tag{B 5}$$

Here we have recovered the chemical potential

$$G=\frac{\partial f_m}{\partial\phi}-\nabla\cdot\frac{\partial f_m}{\partial\nabla\phi} \tag{B 6}$$

and the stress term due to surface tension

$$\boldsymbol{\tau}_\phi=f_m\boldsymbol{I}-\frac{\partial f_m}{\partial\nabla\phi}\otimes\nabla\phi. \tag{B 7}$$

The surface tension term (B 7) can also be obtained by the virtual work principle without imposing the incompressibility condition. Considering the conserved phase dynamics (B 4), (B 5) can be further written as

$$\frac{\mathrm{d}}{\mathrm{d}t}\int_\Omega f_m\,\mathrm{d}\boldsymbol{x}=\int_\Omega\left(\nabla G\cdot\boldsymbol{j}+\boldsymbol{\tau}_\phi:\nabla\boldsymbol{u}\right)\mathrm{d}\boldsymbol{x}+\oint_{\partial\Omega}\left(\boldsymbol{n}\cdot\frac{\partial f_m}{\partial\nabla\phi}\right)\frac{\mathrm{D}\phi}{\mathrm{D}t}\,\mathrm{d}s, \tag{B 8}$$

where we have used the condition $\boldsymbol{n}\cdot\boldsymbol{j}=0$ on $\partial\Omega$.

https://doi.org/10.1017/jfm.2020.465 Published online by Cambridge University Press

For the kinetic energy, we get

$$\begin{aligned}\frac{\mathrm{d}}{\mathrm{d}t}\int_\Omega \frac{1}{2}\rho|\boldsymbol{u}|^2\,\mathrm{d}\boldsymbol{x} &= \int_\Omega \left[\frac{\partial}{\partial t}\left(\rho\frac{|\boldsymbol{u}|^2}{2}\right)+\nabla\cdot\left(\boldsymbol{u}\rho\frac{|\boldsymbol{u}|^2}{2}\right)\right]\mathrm{d}\boldsymbol{x}\\ &= \int_\Omega \left[\rho\frac{\partial \boldsymbol{u}}{\partial t}\cdot\boldsymbol{u}+\rho\boldsymbol{u}\cdot(\nabla\boldsymbol{u})\cdot\boldsymbol{u}+\frac{|\boldsymbol{u}|^2}{2}\left(\frac{\partial\rho}{\partial t}+\nabla\cdot(\rho\boldsymbol{u})\right)\right]\mathrm{d}\boldsymbol{x}\\ &= \int_\Omega \rho\frac{\mathrm{D}\boldsymbol{u}}{\mathrm{D}t}\cdot\boldsymbol{u}\,\mathrm{d}\boldsymbol{x}=\int_\Omega(\nabla\cdot\boldsymbol{T})\cdot\boldsymbol{u}\,\mathrm{d}\boldsymbol{x}\\ &= \oint_{\partial\Omega}\boldsymbol{n}\cdot\boldsymbol{T}\cdot\boldsymbol{u}\,\mathrm{d}s-\int_\Omega\boldsymbol{T}:\nabla\boldsymbol{u}\,\mathrm{d}\boldsymbol{x},\end{aligned}\tag{B 9}$$

where we have used (B 2) in the third equality and (B 3) in the fourth equality.

Different from the mixing and kinetic energies, the wall energy is associated with the solid wall and is thus advected by $\boldsymbol{u}_w$ instead of $\boldsymbol{u}$. Since the wall surface is rigid (thus, the surface divergence of $\boldsymbol{u}_w$ vanishes), we have

$$\begin{aligned}\frac{\mathrm{d}}{\mathrm{d}t}\int_{\partial\Omega_w} f_w\,\mathrm{d}s &= \int_{\partial\Omega_w}\left(\frac{\partial f_w}{\partial t}+\boldsymbol{u}_w\cdot\nabla f_w\right)\mathrm{d}s\\ &= \int_{\partial\Omega_w}\left[f_w'(\phi)\frac{\mathrm{D}\phi}{\mathrm{D}t}-f_w'(\phi)\boldsymbol{u}_s\cdot\nabla\phi\right]\mathrm{d}s,\end{aligned}\tag{B 10}$$

where we have used the relation $\boldsymbol{u}_s=\boldsymbol{u}-\boldsymbol{u}_w$.

Summing up (B 8), (B 9) and (B 10), we arrive at the energy equation

$$\begin{aligned}\frac{\mathrm{d}}{\mathrm{d}t}\mathcal{F} &= \int_\Omega\left[\nabla G\cdot\boldsymbol{j}-(\boldsymbol{T}-\boldsymbol{\tau}_\phi):\nabla\boldsymbol{u}\right]\mathrm{d}\boldsymbol{x}\\ &+\int_{\partial\Omega_w}\left[\left(\boldsymbol{n}\cdot\frac{\partial f_m}{\partial\nabla\phi}+f_w'(\phi)\right)\frac{\mathrm{D}\phi}{\mathrm{D}t}+(\boldsymbol{n}\cdot\boldsymbol{T}-f_w'(\phi)\nabla\phi)\cdot\boldsymbol{u}_s\right]\mathrm{d}s\\ &+\int_{\partial\Omega_w}\boldsymbol{n}\cdot\boldsymbol{T}\cdot\boldsymbol{u}_w\,\mathrm{d}s+\int_{\partial\Omega\setminus\partial\Omega_w}\boldsymbol{n}\cdot\boldsymbol{T}\cdot\boldsymbol{u}\,\mathrm{d}s+\int_{\partial\Omega\setminus\partial\Omega_w}\boldsymbol{n}\cdot\frac{\partial f_m}{\partial\nabla\phi}\frac{\mathrm{D}\phi}{Dt}\,\mathrm{d}s.\end{aligned}\tag{B 11}$$

Here we have recovered the surface potential on the wall boundary $\partial\Omega_w$:

$$L(\phi,\nabla\phi)=\boldsymbol{n}\cdot\frac{\partial f_m}{\partial\nabla\phi}+f_w'(\phi).\tag{B 12}$$

The first two terms on the right-hand side of (B 11) denote the dissipation rate in the system, which corresponds to entropy production due to irreversible processes. The third and fourth terms account for the work done by the moving wall and other boundaries. The last term vanishes if we impose $\boldsymbol{n}\cdot(\partial f_m/\partial\nabla\phi)=0$ on $\partial\Omega\setminus\partial\Omega_w$, i.e. the interface is perpendicular to the boundary. This corresponds to a neutral wetting condition, which is automatically satisfied if we use homogeneous natural boundary conditions for the Cahn–Hilliard equation on boundaries other than the wall.

The dissipation terms in (B 11) have been written in the form of products of the 'generalized flux' and the corresponding 'generalized force'. According to the second law of thermodynamics, the irreversible processes must be entropy-productive, i.e. the

https://doi.org/10.1017/jfm.2020.465 Published online by Cambridge University Press

associated energy dissipation rate must be non-negative. If we assume linear response then energy dissipation is satisfied if we take

$$\boldsymbol{j} = -M\nabla G \quad \text{in } \Omega, \tag{B 13}$$

$$\boldsymbol{T} = -\mu(\nabla \boldsymbol{u} + (\nabla \boldsymbol{u})^T) + \boldsymbol{\tau}_\phi \quad \text{in } \Omega, \tag{B 14}$$

$$\frac{\mathrm{D}\phi}{\mathrm{D}t} = -\Gamma L \quad \text{on } \partial\Omega_w, \tag{B 15}$$

$$-\beta \boldsymbol{u}_s = (\boldsymbol{n}\cdot\boldsymbol{T} - f_w'(\phi)\nabla\phi)\cdot(\boldsymbol{I} - \boldsymbol{n}\otimes\boldsymbol{n}) \quad \text{on } \partial\Omega_w, \tag{B 16}$$

with some positive parameters M, μ, Γ and β. It should be noted that there might be other energy-dissipative constitutive relations than (B 13)–(B 16) and additional conditions are required to determine the physically correct constitutive relations. In (B 14) we have assumed that $\boldsymbol{T} - \boldsymbol{\tau}_\phi$ is a symmetric tensor, which is usually the case for physically relevant systems. In (B 16) we have used $\boldsymbol{u}_s = (\boldsymbol{I} - \boldsymbol{n}\otimes\boldsymbol{n})\cdot\boldsymbol{u}_s$ which is a direct result of the impermeability condition $\boldsymbol{n}\cdot\boldsymbol{u}_s = 0$.

Plugging (B 13) into (B 4), we arrive at the Cahn–Hilliard equation

$$\frac{\mathrm{D}\phi}{\mathrm{D}t} = \nabla\cdot(M\nabla G), \tag{B 17}$$

where M is called the mobility parameter.

For incompressible flows, $\boldsymbol{I} : \nabla\boldsymbol{u} = \nabla\cdot\boldsymbol{u} = 0$; thus, an isotropic term $-p\boldsymbol{I}$ can be added to $\boldsymbol{T}$ without affecting dissipation. This parameter p, interpreted as pressure, serves as a Lagrange multiplier to enforce incompressibility. The momentum equation (B 3) thus reads as

$$\rho\frac{D\boldsymbol{u}}{\mathrm{D}t} = \nabla\cdot\left[-p\boldsymbol{I} + \mu\left(\nabla\boldsymbol{u} + (\nabla\boldsymbol{u})^T\right) + \boldsymbol{\tau}_\phi\right]. \tag{B 18}$$

It should be noted that different forms of $\boldsymbol{\tau}_\phi$ have been used in the literature. For example, the isotropic term $f_m\boldsymbol{I}$ can be absorbed into $p\boldsymbol{I}$ such that one can effectively use $\tilde{\boldsymbol{\tau}}_\phi = -\partial f_m/\partial\nabla\phi\otimes\nabla\phi$ to replace $\boldsymbol{\tau}_\phi$ (Yue *et al.* 2004). The forcing term due to $\boldsymbol{\tau}_\phi$ can also be written as

$$\begin{aligned}\nabla\cdot\boldsymbol{\tau}_\phi &= \nabla f_m - \nabla\cdot\left(\frac{\partial f_m}{\partial\nabla\phi}\otimes\nabla\phi\right)\\ &= \left(\frac{\partial f_m}{\partial\phi}\nabla\phi + \frac{\partial f_m}{\partial\nabla\phi}\cdot\nabla\nabla\phi\right) - \left[\left(\nabla\cdot\frac{\partial f_m}{\partial\nabla\phi}\right)\nabla\phi + \frac{\partial f_m}{\partial\nabla\phi}\cdot\nabla\nabla\phi\right]\\ &= G\nabla\phi,\end{aligned} \tag{B 19}$$

which is adopted in this work. Alternatively, a body force of the form $-\phi\nabla G = G\nabla\phi - \nabla(G\phi)$ was also found in the literature (Jacqmin 2000).

On the solid wall, the wall energy relaxation is governed by (B 15). Equation (B 16) is exactly the generalized Navier boundary condition (Qian, Wang & Sheng 2006*a*; Qian *et al.* 2006*b*), which was originally derived based on Onsager's principle of minimum energy dissipation. It should be noted that the no-slip condition $\boldsymbol{u}_s = 0$, adopted by us and many others (Jacqmin 2000; Khatavkar *et al.* 2007*b*; Carlson, Do-Quang & Amberg 2009), provides a simpler formulation which also satisfies energy dissipation.

https://doi.org/10.1017/jfm.2020.465 Published online by Cambridge University Press

Appendix C. Compressibility and Mass diffusion

For incompressible flows, we usually impose $\nabla \cdot \boldsymbol{u} = 0$. The mixture density ρ is governed by mass conservation (B 2). Meanwhile, given the densities of the pure phases, the mixture density can also be expressed as a function of the phase-field variable ϕ, and is therefore governed by the phase-field equation (B 17) unless $\rho'(\phi) = 0$. Thus, the system in appendix B. may be over-determined if the two phases have different densities. To remedy this, the governing equations need to be modified and there are primarily two ways to derive physically consistent models.

The first method, proposed by Lowengrub & Truskinovsky (1998), is to consider the system as quasi-incompressible. In this treatment, ϕ is associated with mass fraction and the mixture velocity $\boldsymbol{u}$ is interpreted as the mass-averaged velocity. Then, from mass conservation (B 2), we can obtain

$$\nabla \cdot \boldsymbol{u} = -\frac{1}{\rho}\frac{\mathrm{D}\rho}{\mathrm{D}t} = -\frac{\rho'(\phi)}{\rho}\frac{\mathrm{D}\phi}{\mathrm{D}t}, \tag{C 1}$$

where $\mathrm{D}\phi/\mathrm{D}t$ is determined by the Cahn–Hilliard equation. This equation replaces the original $\nabla \cdot \boldsymbol{u} = 0$. Moreover, due to compressibility, the mixing energy f_m has to be interpreted as a free energy per unit mass (and, thus, the total mixing energy is $\int_\Omega \rho f_m \,\mathrm{d}\boldsymbol{x}$), which will cause substantial changes to the governing equations. Applications of this method can be found in Guo, Lin & Lowengrub (2014) and Guo & Lin (2015).

The other method, first proposed by Ding, Spelt & Shu (2007) and later improved by Abels *et al.* (2012), associates ϕ with volume fraction and interprets $\boldsymbol{u}$ as the volume-averaged velocity. It can be easily shown that $\nabla \cdot \boldsymbol{u} = 0$ is still satisfied. However, this volume-averaged velocity modifies the mass conservation equation (B 2) to

$$\frac{\partial \rho}{\partial t} + \nabla \cdot (\rho \boldsymbol{u}) + \nabla \cdot \boldsymbol{J} = 0, \tag{C 2}$$

where $\boldsymbol{J}$ is the diffusive mass flux. It is obvious that

$$\nabla \cdot J = -\frac{\mathrm{D}\rho}{\mathrm{D}t} = -\rho'(\phi)\frac{\mathrm{D}\phi}{\mathrm{D}t}. \tag{C 3}$$

Comparing this equation with (B 4) and considering the fact that $\rho'(\phi)$ is usually a constant (see (2.16) for an example), we arrive at the identity

$$\boldsymbol{J} = \rho'(\phi)\boldsymbol{j}. \tag{C 4}$$

Considering (C 2) and the Galilean invariance requirement, the momentum equation (B 3) is updated to

$$\rho\frac{\mathrm{D}\boldsymbol{u}}{\mathrm{d}t} + \boldsymbol{J} \cdot \nabla \boldsymbol{u} = \nabla \cdot \tilde{\boldsymbol{T}}, \tag{C 5}$$

where $\tilde{\boldsymbol{T}} = \boldsymbol{T} + \boldsymbol{J} \otimes \boldsymbol{u}$ is an objective tensor that replaces the original $\boldsymbol{T}$ in (B 3). The interested reader may refer to Abels *et al.* (2012) for detailed derivations and Dong (2014, 2015) for extensions to N-phase systems with $N \geq 2$. It should be noted that the original formulation in Ding *et al.* (2007) is not Galilean invariant.

The method by Abels *et al.* allows us to use the existing numerical algorithms for incompressible flows with very little modification, and is thus more frequently seen in the recent literature (e.g. Shen & Yang 2015; Yu & Yang 2017). In the following we only focus on this method.

https://doi.org/10.1017/jfm.2020.465 Published online by Cambridge University Press

With the modified mass conservation (C 2) and momentum equation (C 5), the time derivative of kinetic energy is updated to

$$\begin{aligned}\frac{\mathrm{d}}{\mathrm{d}t}\int_\Omega \frac{1}{2}\rho|\boldsymbol{u}|^2\,\mathrm{d}\boldsymbol{x} &= \int_\Omega \left[\frac{|\boldsymbol{u}|^2}{2}\left(\frac{\partial\rho}{\partial t}+\nabla\cdot(\rho\boldsymbol{u})\right)+\rho\frac{\mathrm{D}\boldsymbol{u}}{\mathrm{D}t}\cdot\boldsymbol{u}\right]\mathrm{d}\boldsymbol{x}\\ &= \int_\Omega \left[-\frac{|\boldsymbol{u}|^2}{2}\nabla\cdot\boldsymbol{J}+(\nabla\cdot\tilde{\boldsymbol{T}}-\boldsymbol{J}\cdot\nabla\boldsymbol{u})\cdot\boldsymbol{u}\right]\mathrm{d}\boldsymbol{x}\\ &= \oint_{\partial\Omega}\left(-\boldsymbol{n}\cdot\boldsymbol{J}\frac{|\boldsymbol{u}|^2}{2}+\boldsymbol{n}\cdot\tilde{\boldsymbol{T}}\cdot\boldsymbol{u}\right)\mathrm{d}s-\int_\Omega\tilde{\boldsymbol{T}}:\nabla\boldsymbol{u}\,\mathrm{d}\boldsymbol{x}\\ &= \oint_{\partial\Omega}\boldsymbol{n}\cdot\tilde{\boldsymbol{T}}\cdot\boldsymbol{u}\,\mathrm{d}s-\int_\Omega\tilde{\boldsymbol{T}}:\nabla\boldsymbol{u}\,\mathrm{d}\boldsymbol{x},\end{aligned}\tag{C 6}$$

where we have used the zero-diffusive-flux condition $\boldsymbol{n}\cdot\boldsymbol{J}=\rho'(\phi)\boldsymbol{n}\cdot\boldsymbol{j}=0$ on the boundary. This equation is identical to (B 9) except for a different interpretation of the stress tensor. Consequently, all the equations remain the same as those in appendix B, except for the modified mass conservation and momentum equations.

In our computations on oscillating drops (see figure 17*d*), however, we did not find any noticeable difference between the results from (B 3) and (C 5). Thus, in practice, the effect of compressibility is only limited to the diffuse interface and has negligible effect on the macroscopic flow.

REFERENCES

ABELS, H., GARCKE, H. & GRÜN, G. 2012 Thermodynamically consistent, frame indifferent diffuse interface models for incompressible two-phase flows with different densities. *Math. Models Meth. Appl. Sci.* **22** (03), 1150013.

AFKHAMI, S., BUONGIORNO, J., GUION, A., POPINET, S., SAADE, Y., SCARDOVELLI, R. & ZALESKI, S. 2018 Transition in a numerical model of contact line dynamics and forced dewetting. *J. Comput. Phys.* **374**, 1061–1093.

AFKHAMI, S., ZALESKI, S. & BUSSMANN, M. 2009 A mesh-dependent model for applying dynamic contact angles to VOF simulations. *J. Comput. Phys.* **228**, 5370–5389.

ALZETTA, G., ARNDT, D., BANGERTH, W., BODDU, V., BRANDS, B., DAVYDOV, D., GASSMOELLER, R., HEISTER, T., HELTAI, L., KORMANN, K., *et al.*2018 The deal.II library, version 9.0. *J. Numer. Maths* **26** (4), 173–183.

BA, Y., LIU, H., SUN, J. & ZHENG, R. 2013 Color-gradient lattice Boltzmann model for simulating droplet motion with contact-angle hysteresis. *Phys. Rev.* E **88**, 043306.

BANGERTH, W. 2000 Using modern features of C++ for adaptive finite element methods: dimension-independent programming in deal.II. In *Proceedings of the 16th IMACS World Congress 2000, Lausanne, Switzerland* (ed. M. Deville & R. Owens). International Association for Mathematics and Computers in Simulation.

BANGERTH, W., HARTMANN, R. & KANSCHAT, G. 2007 deal.II—a general purpose object oriented finite element library. *ACM Trans. Math. Softw.* **33** (4), 24.

CAHN, J. W. 1977 Critical-point wetting. *J. Chem. Phys.* **66**, 3667–3672.

CAHN, J. W. & HILLIARD, J. E. 1958 Free energy of a nonuniform system. Part 1. Interfacial free energy. *J. Chem. Phys.* **28**, 258–267.

CARLSON, A., DO-QUANG, M. & AMBERG, G. 2009 Modeling of dynamic wettting far from equilibrium. *Phys. Fluids* **21**, 121701.

CARLSON, A., DO-QUANG, M. & AMBERG, G. 2011 Dissipation in rapid dynamic wetting. *J. Fluid Mech.* **682**, 213–240.

COX, R. G. 1986 The dynamics of the spreading of liquids on a solid surface. Part 1. Viscous flow. *J. Fluid Mech.* **168**, 169–194.

https://doi.org/10.1017/jfm.2020.465 Published online by Cambridge University Press

DAVIS, T. A. 2004 Algorithm 832: Umfpack v4.3—an unsymmetric-pattern multifrontal method. *ACM Trans. Math. Softw.* **30** (2), 196–199.

DING, H. & SPELT, P. D. M. 2008 Onset of motion of a three-dimensional droplet on a wall in shear flow at moderate Reynolds numbers. *J. Fluid Mech.* **599**, 341–362.

DING, H., SPELT, P. D. M. & SHU, C. 2007 Diffuse interface model for incompressible two-phase flows with large density ratios. *J. Comput. Phys.* **226** (2), 2078–2095.

DONG, S. 2014 An efficient algorithm for incompressible N-phase flows. *J. Comput. Phys.* **276**, 691–728.

DONG, S. 2015 Physical formulation and numerical algorithm for simulating n immiscible incompressible fluids involving general order parameters. *J. Comput. Phys.* **283**, 98–128.

DU, Q. & NICOLAIDES, R. 1991 Numerical analysis of a continuum model of phase transition. *SIAM J. Numer. Anal.* **28** (5), 1310–1322.

DUPONT, J.-B. & LEGENDRE, D. 2010 Numerical simulation of static and sliding drop with contact angle hysteresis. *J. Comput. Phys.* **229** (7), 2453–2478.

DUSSAN V., E. B. 1979 On the spreading of liquids on solid surfaces: static and dynamic contact lines. *Annu. Rev. Fluid Mech.* **11**, 371–400.

DUSSAN V., E. B. & CHOW, R. T.-P. 1983 On the ability of drops or bubbles to stick to non-horizontal surfaces of solids. *J. Fluid Mech.* **137**, 1–29.

ERAL, B., 'T MANNETJE, D. & OH, J. 2013 Contact angle hysteresis: a review of fundamentals and applications. *Colloid Polym. Sci.* **291** (2), 247–260.

EXTRAND, C. W. 2002 Model for contact angles and hysteresis on rough and ultraphobic surfaces. *Langmuir* **18** (21), 7991–7999.

EXTRAND, C. W. 2016 Origins of wetting. *Langmuir* **32** (31), 7697–7706.

EYRE, D. J. 1998 Unconditionally gradient stable time marching the Cahn–Hilliard equation. In *Computational and Mathematical Models of Microstructural Evolution (San Francisco, CA, 1998)*, Materials Research Society Symposium Proceedings, vol. 529, pp. 39–46. Materials Research Society.

FERNÁNDEZ-TOLEDANO, J.-C., BLAKE, T., LIMAT, L. & DE CONINCK, J. 2019 A molecular-dynamics study of sliding liquid nanodrops: dynamic contact angles and the pearling transition. *J. Colloid Interface Sci.* **548**, 66–76.

FURMIDGE, C. 1962 Studies at phase interfaces. I. The sliding of liquid drops on solid surfaces and a theory for spray retention. *J. Colloid Sci.* **17** (4), 309–324.

GAO, L. & MCCARTHY, T. J. 2006 Contact angle hysteresis explained. *Langmuir* **22** (14), 6234–6237.

GAO, M. & WANG, X.-P. 2014 An efficient scheme for a phase field model for the moving contact line problem with variable density and viscosity. *J. Comput. Phys.* **272**, 704–718.

DE GENNES, P. G. & PROST, J. 1993 *The Physics of Liquid Crystals*, 2nd edn. Oxford University Press.

GOMEZ, H. & VAN DER ZEE, K. G. 2017 Computational phase-field modeling. In *Encyclopedia of Computational Mechanics*, 2nd edn, pp. 1–35. American Cancer Society.

GUERMOND, J.-L. & QUARTAPELLE, L. 2000 A projection FEM for variable density incompressible flows. *J. Comput. Phys.* **165** (1), 167–188.

GUO, Z. & LIN, P. 2015 A thermodynamically consistent phase-field model for two-phase flows with thermocapillary effects. *J. Fluid Mech.* **766**, 226–271.

GUO, Z., LIN, P. & LOWENGRUB, J. 2014 A numerical method for the quasi-incompressible Cahn–Hilliard-Navier–Stokes equations for variable density flows with a discrete energy law. *J. Comput. Phys.* **276**, 486–507.

HEISTER, T. & RAPIN, G. 2013 Efficient augmented lagrangian-type preconditioning for the Oseen problem using Grad-DIV stabilization. *Intl J. Numer. Meth. Fluids* **71** (1), 118–134.

HOFFMAN, R. L. 1975 A study of the advancing interface. *J. Colloid Interface Sci.* **50**, 228–241.

HUANG, J.-J., HUANG, H. & WANG, X. 2014 Numerical study of drop motion on a surface with stepwise wettability gradient and contact angle hysteresis. *Phys. Fluids* **26** (6), 062101.

IWAMATSU, M. 2006 Contact angle hysteresis of cylindrical drops on chemically heterogeneous striped surfaces. *J. Colloid Interface Sci.* **297** (2), 772–777.

JACQMIN, D. 1999 Calculation of two-phase Navier–Stokes flows using phase-field modeling. *J. Comput. Phys.* **155** (1), 96–127.

JACQMIN, D. 2000 Contact-line dynamics of a diffuse fluid interface. *J. Fluid Mech.* **402**, 57–88.

https://doi.org/10.1017/jfm.2020.465 Published online by Cambridge University Press

JANARDAN, N. & PANCHAGNULA, M. V. 2014 Effect of the initial conditions on the onset of motion in sessile drops on tilted plates. *Colloids Surf.* A **456**, 238–245.

KHATAVKAR, V. V., ANDERSON, P. D., DUINEVELD, P. C. & MEIJER, H. E. H. 2007*a* Diffuse-interface modelling of droplet impact. *J. Fluid Mech.* **581**, 97–127.

KHATAVKAR, V. V., ANDERSON, P. D. & MEIJER, H. E. H. 2007*b* Capillary spreading of a droplet in the partially wetting regime using a diffuse-interface model. *J. Fluid Mech.* **572**, 367–387.

KUSUMAATMAJA, H. & YEOMANS, J. M. 2007 Modeling contact angle hysteresis on chemically patterned and superhydrophobic surfaces. *Langmuir* **23** (11), 6019–6032.

LINDER, N., CRISCIONE, A., ROISMAN, I. V., MARSCHALL, H. & TROPEA, C. 2015 3D computation of an incipient motion of a sessile drop on a rigid surface with contact angle hysteresis. *Theor. Comput. Fluid Dyn.* **29** (5), 373–390.

LIU, H., JU, Y., WANG, N., XI, G. & ZHANG, Y. 2015 Lattice Boltzmann modeling of contact angle and its hysteresis in two-phase flow with large viscosity difference. *Phys. Rev.* E **92**, 033306.

LOWENGRUB, J. & TRUSKINOVSKY, L. 1998 Quasi-incompressible Cahn–Hilliard fluids and topological transitions. *Proc. R. Soc. Lond.* A **454** (1978), 2617–2654.

LUO, L., WANG, X.-P. & CAI, X.-C. 2017 An efficient finite element method for simulation of droplet spreading on a topologically rough surface. *J. Comput. Phys.* **349**, 233–252.

MAGLIO, M. & LEGENDRE, D. 2014 Numerical simulation of sliding drops on an inclined solid surface. In *Computational and Experimental Fluid Mechanics with Applications to Physics, Engineering and the Environment* (ed. L. Di G. Sigalotti, J. Klapp & E. Sira), pp. 47–69. Springer International Publishing.

MAKKONEN, L. 2017 A thermodynamic model of contact angle hysteresis. *J. Chem. Phys.* **147** (6), 064703.

METZGER, S. 2019 On stable, dissipation reducing splitting schemes for two-phase flow of electrolyte solutions. *Numer. Algorithms* **80** (4), 1361–1390.

PRABHALA, B., PANCHAGNULA, M. V. & VEDANTAM, S. 2013 Three-dimensional equilibrium shapes of drops on hysteretic surfaces. *Colloid Polym. Sci.* **291**, 279–289.

QIAN, T., WANG, X.-P. & SHENG, P. 2003 Molecular scale contact line hydrodynamics of immiscible flows. *Phys. Rev.* E **68**, 016306.

QIAN, T., WANG, X.-P. & SHENG, P. 2006*a* Molecular hydrodynamics of the moving contact line in two-phase immiscible flows. *Commun. Comput. Phys.* **1**, 1–52.

QIAN, T., WANG, X.-P. & SHENG, P. 2006*b* A variational approach to moving contact line hydrodynamics. *J. Fluid Mech.* **564**, 333–360.

QUÉRÉ, D. 2008 Wetting and roughness. *Annu. Rev. Mater. Res.* **38** (1), 71–99.

RAHIMI, P. & WARD, C. A. 2005 Contact angle hysteresis on smooth and homogenous surfaces in gravitational fiel ds. *Microgravity Sci. Technol.* **16** (1), 231–235.

REN, W. & E, W. 2007 Boundary conditions for the moving contact line problem. *Phys. Fluids* **19**, 022101.

REN, W. & E, W. 2011*a* Contact line dynamics on heterogeneous surfaces. *Phys. Fluids* **23**, 072103.

REN, W. & E, W. 2011*b* Derivation of continuum models for the moving contact line problem based on thermodynamic principles. *Commun. Math. Sci.* **9**, 597–606.

SCHLEIZER, A. D. & BONNECAZE, R. T. 1999 Displacement of a two-dimensional immiscible droplet adhering to a wall in shear and pressure-driven flows. *J. Fluid Mech.* **383**, 29–54.

SHEN, J., XU, J. & YANG, J. 2018 The scalar auxiliary variable (SAV) approach for gradient flows. *J. Comput. Phys.* **353**, 407–416.

SHEN, J. & YANG, X. 2010 Numerical approximations of Allen–Cahn and Cahn–Hilliard equations. *Discrete Continuous Dyn. Syst.* A **28**, 1669–1691.

SHEN, J. & YANG, X. 2015 Decoupled, energy stable schemes for phase-field models of two-phase incompressible flows. *SIAM J. Numer. Anal.* **53** (1), 279–296.

SHEN, J., YANG, X. & YU, H. 2015 Efficient energy stable numerical schemes for a phase field moving contact line model. *J. Comput. Phys.* **284**, 617–630.

SHIN, S., CHERGUI, J. & JURIC, D. 2018 Direct simulation of multiphase flows with modeling of dynamic interface contact angle. *Theor. Comput. Fluid Dyn.* **32** (5), 655–687.

SOUTAS-LITTLE, R. W. 1999 *Elasticity*. Dover.

SPELT, P. D. 2005 A level-set approach for simulations of flows with multiple moving contact lines with hysteresis. *J. Comput. Phys.* **207** (2), 389–404.

https://doi.org/10.1017/jfm.2020.465 Published online by Cambridge University Press

VEDANTAM, S. & PANCHAGNULA, M. V. 2007 Phase field modeling of hysteresis in sessile drops. *Phys. Rev. Lett.* **99**, 176102.

VILLANUEVA, W. & AMBERG, G. 2006 Some generic capillary-driven flows. *Intl J. Multiphase Flow* **32** (9), 1072–1086.

VOINOV, O. V. 1976 Hydrodynamics of wetting. *J. Fluid Mech.* **11** (5), 714–721 (translated from Izvestiya Akademii Nauk SSSR, Mekhanika Zhidkosti i Gaza, No. 5, pp. 76–84, September–October 1976).

WANG, L., HUANG, H.-B. & LU, X.-Y. 2013 Scheme for contact angle and its hysteresis in a multiphase lattice Boltzmann method. *Phys. Rev.* E **87**, 013301.

WHYMAN, G., BORMASHENKO, E. & STEIN, T. 2008 The rigorous derivation of Young, Cassie–Baxter and Wenzel equations and the analysis of the contact angle hysteresis phenomenon. *Chem. Phys. Lett.* **450** (4), 355–359.

WU, S. & MA, M. 2017 A contact angle hysteresis model based on the fractal structure of contact line. *J. Colloid Interface Sci.* **505**, 995–1000.

WYLOCK, C., PRADAS, M., HAUT, B., COLINET, P. & KALLIADASIS, S. 2012 Disorder-induced hysteresis and nonlocality of contact line motion in chemically heterogeneous microchannels. *Phys. Fluids* **24** (3), 032108.

XU, X. & WANG, X. 2011 Analysis of wetting and contact angle hysteresis on chemically patterned surfaces. *SIAM J. Appl. Maths* **71** (5), 1753–1779.

XU, X. & WANG, X. 2013 The modified Cassie's equation and contact angle hysteresis. *Colloid Polym. Sci.* **291** (2), 299–306.

YANG, X. 2016 Linear, first and second order and unconditionally energy stable numerical schemes for the phase field model of homopolymer blends. *J. Comput. Phys.* **302**, 509–523.

YU, H. & YANG, X. 2017 Numerical approximations for a phase-field moving contact line model with variable densities and viscosities. *J. Comput. Phys.* **334**, 665–686.

YUE, P. & FENG, J. J. 2011 Wall energy relaxation in the Cahn–Hilliard model for moving contact lines. *Phys. Fluids* **23**, 012106.

YUE, P., FENG, J. J., LIU, C. & SHEN, J. 2004 A diffuse-interface method for simulating two-phase flows of complex fluids. *J. Fluid Mech.* **515**, 293–317.

YUE, P., ZHOU, C. & FENG, J. J. 2010 Sharp-interface limit of the Cahn–Hilliard model for moving contact lines. *J. Fluid Mech.* **645**, 279–294.

YUE, P., ZHOU, C., FENG, J. J., OLLIVIER-GOOCH, C. F. & HU, H. H. 2006 Phase-field simulations of interfacial dynamics in viscoelastic fluids using finite elements with adaptive meshing. *J. Comput. Phys.* **219**, 47–67.

ZHANG, J. & YUE, P. 2020 A level-set method for moving contact lines with contact angle hysteresis. *J. Comput. Phys.* **418**, 109636.

https://doi.org/10.1017/jfm.2020.465 Published online by Cambridge University Press